LBL-14664

LBL--14664

DE82 020070

ELECTRON PARAMAGNETIC RESONANCE AT DISLOCATIONS IN GERMANIUM

Elga Jekabsons Pakulis

Ph.D. Thesis

June 1982

Materials and Molecular Research Division
Lawrence Berkeley Laboratory
University of California
Berkeley, CA 94720

This work was supported by the Director, Office of Energy Research, Office of Basic Energy Sciences, Materials Sciences Division of the U.S. Department of Energy under Contract No. DE-AC03-76SF00098.

Electron Paramagnetic Resonance
at Dislocations in Germanium

by

Elga Jekabsons Pakulis
Materials and Molecular Research Division
Lawrence Berkeley Laboratory
and
Department of Physics
University of California, Berkeley, Ca

ABSTRACT

The first observation of the paramagnetic resonance of electrons at dislocations in germanium single crystals is reported. Under subband gap optical excitation, two sets of lines are detected: four lines about the <111> axes with $g_{\parallel}=0.34$ and $g_{\perp}=1.94$, and 24 lines with $g_{\parallel}=0.73$ and $g_{\perp}=1.89$ about <111> axes with a six-fold 1.2° distortion. This represents the first measurement of the distortion angle of a dislocation dangling bond. The possibility that the distortion results from a Peierls transition along the dislocation line is discussed. An electric detection technique was used. This involved monitoring the absorption of energy from the microwave electric field by photo-excited electrons. Due to spin dependent scattering of the

electrons by dislocation dangling bonds, a resonant change in this absorption was observed on each passage through spin resonance. Both increases and decreases in the absorption were observed, depending on crystal growth conditions. The spin dependent scattering was observed to persist for hours after the removal of optical excitation, indicating the existence of a very long lifetime, conducting dislocation band. In a lithium diffused germanium crystal containing dislocations, a different spectrum was observed, with principal g values 1.917, 1.896, and 0.855, along the axes $\langle 110\rangle$, $\langle 1\bar{1}\bar{2}\rangle$, and $\langle 1\bar{1}1\rangle$, plus equivalent sets. This spectrum is attributed to a dangling bond - lithium ion complex. The experiments were conducted on a 1-cm superheterodyne spectrometer, using liquid helium cooled, microwave resonant germanium samples with a high quality factor $Q \simeq 10^5$. It was the ultra-high sensitivity of the self resonant samples coupled with electric detection of magnetic resonance which made possible this study of the very low concentrations of dislocations occurring in as-grown, as opposed to plastically deformed, germanium crystals.

Table of Contents

CHAPTER I - INTRODUCTION

Electron paramagnetic resonance (EPR) (1) has been used widely, and with a great deal of success, in the study of defects in semiconductors. Valuable information can be obtained not only about the identity of a defect, but sometimes also about its microscopic structure. Corbett etal (2) give a good breakdown of the extent to which this powerful technique has been utilized in studies of a long list of semiconductors. Of the elemental semiconductors, silicon has been most extensively studied, while germanium, by comparison, has had strikingly few reports of EPR spectra. The primary reason for this is the inhomogeneous broadening of lines in germanium which leads to a reduction in signal amplitude. The broadening results from unresolved hyperfine structure of the Ge^{73} nucleus, with a spin $I=9/2$ and an isotopic abundance of 7.76%, and, even more importantly, from nonuniform strains in the crystal. The strain broadening is a direct result of the large spin - orbit interaction in Ge.(3) The present work shows that these difficulties are not insurmountable and that we can expect to see the continued successful application of EPR to the study of defects in germanium.

A number of interesting features have surfaced during the course of this work. First of all, I have observed spin-dependent photoconductivity in the germanium samples containing dislocations. Spin-dependent photoconductivity arises when the number and/or the mobility of photo-excited free carriers depends on their spin orientation relative to that of their recombination and/or scattering centers. Secondly, I discovered that the spin-dependent conductivity remains long after the removal of optical excitation. This observation led to the conclusion that free carriers can relax into a long lifetime dislocation band, retaining a non-zero, spin-dependent, mobility. Thirdly, the spin-dependent conductivity along dislocations enabled me to measure the g-tensor of the dislocation dangling bond electrons using the method of electric detection of magnetic resonance. In this method the mobile charges are accelerated by a microwave electric field, their absorption of energy being directly related to their spin polarization (relative to that of their scattering centers, i.e. dangling bond electrons) through their spin-dependent conductivity. The fourth point, and perhaps the most significant result of my thesis is the determination of a small, very well-defined distortion angle of the dislocation dangling bonds. This determination was made directly from the symmetry, multiplicity, and splitting of the lines in the EPR spectrum. There is the intriguing possibility that the distortion of the dangling bonds may be the result of a Peierls transition along the dislocation line. Finally, I have also observed a new spectrum in a lithium diffused germanium crystal containing dislocations, arising from lithium at dislocations.

Before going any further, it will be helpful to briefly discuss dislocations in the tetrahedral crystal structure. Dislocation lines are characterized by a Burgers vector giving the magnitude and direction of the displacement of one part of the crystal relative to the rest of the crystal. The part of the Burgers vector parallel to the dislocation is the screw component, that part perpendicular to the dislocation is the edge component. The two extreme cases - 100 percent screw and 100 percent edge are illustrated in Figure I.1. In the diamond structure, dislocation lines run along <110> directions and often have Burgers vectors at 60° (4). These are the so-called 60°-dislocations and have been studied extensively (5). They can occur in at least two basic varieties, the shuffle set and the glide set, depending on which set of bonds were broken in the creation of the dislocation. If the bonds broken were perpendicular to the dislocation line, one ends up with the shuffle set; otherwise, one has the glide set. This simple picture is helpful conceptually, but in real crystals one encounters many complications, the details of which are not entirely understood. For example, one can have kinks in dislocation lines, or, lines of the shuffle set can become associated with stacking faults, or, lines of the glide set can dissociate into partial dislocations – so long as the sum of the Burgers vectors of the partials equals the Burgers vector of the original line. For the purposes of discussion, the model adopted here is that of the 60°-dislocation of the shuffle set, pictured in Figure I.2. The figure shows the Burgers vector, $\vec{b}$, and the dislocation line, d, with its row of broken bonds. These are the so-called dislocation dangling bonds, which to first order can be thought of as sp^3 orbitals, each containing one electron with spin 1/2.

It has been expected for three decades that the dislocation dangling bond electrons should be observable using magnetic resonance techniques. It was not until 1965 that Alexander, Labusch, and Sander (6) first observed electron spin resonance at dislocation dangling bonds in silicon. The silicon had been plastically deformed to increase the number of dislocations to a density of $\sim 10^8$ cm^{-2}. Why wasn't something similar seen in germanium? One possibility is that plastic deformation of germanium, although resulting in high densities of dislocations, may not increase the amplitude of the signal enough to make it observable, due to increased strain broadening. Throughout this work, only as-grown crystals were studied, with dislocation densities $\sim 10^4$ cm^{-2}.

Without the aid of large numbers of artificially induced dislocations, one needs several orders of magnitude greater sensitivity to detect the spin resonance of the dislocation dangling bond electrons. This greater sensitivity was achieved through the use of high-Q microwave resonant samples and electric detection of magnetic resonance.

The following sections of this thesis treat fully the experimental methods, experimental results, detailed analysis, and conclusions.

CHAPTER II - EXPERIMENTAL DETAILS

II.1 - APPARATUS

All experiments were conducted on the K-band superheterodyne spectrometer described by J. P. Wolfe in his thesis (1), and pictured in Figure II.1. The source klystron was an OKI 24V11S with output power 0.5 watts and frequency range from 22.0 to 26.0 GHz. The power actually reaching the sample could be varied over 10 orders of magnitude using variable attenuators mounted along the waveguide. The signal reflected from the cavity was mixed with that from the local oscillator klystron, an OKI 24V10A with output power 0.3 watts and frequency range 22.0 to 26.0 GHz. Amplification after mixing was achieved using Radiation Devices model BBA-1 Broadband Amplifiers. Final detection was made at the difference frequency of the two klystrons by a Radiation Devices CRD-2 RF Detector. Mixer response was peaked at $|\Delta f| = 30$ MHz. Magnetic field modulation and lock-in amplification were used.

Figures II.2 and II.3 show the dimensions of the inside of the dewar and of that portion of the waveguide inserted into the dewar. Figure II.4 is a blowup of the end of the waveguide together with a cross section of the tunable cylindrical cavity. Optical pumping was possible through a window at the bottom of the dewar and a hole in the bottom of the cavity. A PEK 203 mercury vapor arc lamp was used with/without some combination of the filters listed in Table II.1. With no filters, 0.1 watts reached the sample. An aluminum shutter was mounted directly beneath the cavity in the helium bath and could be rotated from outside the dewar via a stainless steel rod. This allowed the measurement of the dark spectrum and of the decay of the light-induced spectrum. The cavity was centered between the pole pieces of the magnet, which could be rotated in the horizontal plane. The field was measured with a rotating coil gaussmeter, and had an upper limit of 19 kgauss. Calibration was achieved using a g-marker of powdered phosphorous doped silicon embedded in polyethylene, provided by E. A. Gere. All experiments were performed with the sample immersed in liquid helium, usually at temperatures 1.8-1.9 K achieved by mechanically pumping the helium vapor.

II.2 - SAMPLES

I cut samples from Czochralski grown single crystals of lightly doped n-type germanium supplied by W. L. Hansen and E. E. Haller of Lawrence Berkeley Laboratory. Most of the samples were cut in the shape of right circular cylinders using an ultrasonic cutter. They had diameters of 12.5 mm and heights ranging from 8 to 10 mm. The axis of the cylinder was chosen to be either a <100> or a <110> crystal axis. A few of the samples were rectangular parallelopipeds. Results were insensitive to surface preparation.

Table II.2 summarizes sample characteristics. Net donor concentrations were in the range 5×10^9 to 8×10^{13} cm^{-3}. With the exception of one dislocation-free sample, dislocation etch pit densities were between 10^3 and 10^5 cm^{-2}, but were not uniform and should only be regarded as order of magnitude estimates. Diverse crystal growing conditions were selected to study which factors did or did not influence the results. All S- crystals (see Table II.2) were grown in one crystal growing apparatus, the rest of the crystals in another. The growth axes of the crystals were either <100> or <111>, the growth atmospheres were hydrogen, deuterium, argon, or vacuum, and the crucible materials were either quartz or graphite.

The typical sample was lapped, chemically etched, and mounted with styrofoam in the spectrometer cavity. When cooled to liquid helium temperatures, the sample itself becomes a microwave resonant dielectric cavity with a large quality factor $Q \sim 10^5$ (2). This high Q was essential in achieving the required sensitivity.

II.3 - EXPERIMENTAL GEOMETRY

Two different experimental geometries were used, as shown in Figure II.5. Most often the magnetic field was rotated in a plane nearly parallel to a (110) plane of the crystal, which is the only plane containing all three principal directions - <100>, <110>, and <111>. In the second geometry, the field was rotated in a (100) plane. The orientation of the four tetrahedral bonding directions is indicated in the figure. The angle between the magnetic field and these four axes was determined by observing the angular dependence of the electron cyclotron resonance in the sample.

Before discussing the experimental results, I will first describe the technique of electric detection of magnetic resonance.

CHAPTER III - ELECTRIC DETECTION OF MAGNETIC RESONANCE

Electric detection of magnetic resonance is most easily introduced by analogy to the widely used technique of optical detection of magnetic resonance (1). In the latter, one observes the spin resonance of two species giving rise to recombination luminescence by monitoring some aspect of the luminescence (i.e. intensity or polarization) which depends on the spin polarization of the species. In electric detection, instead of looking at spin-dependent luminescence, one looks at spin-dependent conductivity.

The sample is placed in the microwave cavity of an EPR spectrometer. Optical pumping is used, if necessary , to excite conduction electrons. If the conductivity changes during spin resonance so does the absorption by the free carriers, of energy from the microwave electric field. It is this change in absorption which is detected as a change in cavity Q, and in general it can be of either sign. If the conductivity increases, the absorption increases and the Q decreases as for an ordinary absorptive signal. If the conductivity decreases, the absorption decreases and the Q increases as for an emissive signal.

Dependence of the conductivity on spin polarization can result from spin dependent scattering processes and/or spin dependent recombination processes. Numerous examples of this effect can be found in the literature. Honig considered the neutral impurity scattering of highly spin-polarized carriers in semiconductors (2). He suggested that Zeeman spectroscopy of the neutral shallow donors could be carried out by observing changes in photo-conductivity occurring during changes in spin polarization. Maxwell and Honig did the experiment for the case of the phosphorus donor in silicon.

The basic idea involved is that the triplet scattering cross-section (carrier and scatterer have parallel spins) differs from the singlet scattering cross-section (carrier and scatterer have anti-parallel spins), and the percentage of triplet scattering events is a function of the spin polarization. The net result is that the conductivity is spin dependent because the mobility of carriers is a function of spin polarization.

For a more quantitative description, consider the following simple model. Let

$n=n\uparrow+n\downarrow$=concentration of mobile electrons with spin 1/2

$N=N\uparrow+N\downarrow$=concentration of scattering centers with spin

1/2

$p=(n\uparrow-n\downarrow)/n$=spin polarization of mobile electrons

$P=(N\uparrow-N\downarrow)/N$=spin polarization of scattering centers

Xs=singlet scattering cross section

Xt=triplet scattering cross section

The probability of singlet scattering is given by

$$(n\uparrow N\downarrow+n\downarrow N\uparrow)/(2nN)=$$

$$(n/2(1-p)N/2(P+1)+n/2(p+1)N/2(1-P))/\ (2nN)=$$

$$(1-pP)/4 \qquad \text{(III.1)}$$

The probability of triplet scattering is

$$1-(1-pP)/4=$$

$$(3+pP)/4 \qquad \text{(III.2)}$$

so that the total scattering cross section is just

$$X=Xs(1-pP)/4+Xt(3+pP)/4. \qquad \text{(III.3)}$$

The conductivity is proportional to $1/X$. If either one of the spin transitions is saturated, ie $p=0$ or $P=0$, the change in X is $pP(Xs-Xt)/4$ and the fractional change in conductivity is

$$\Delta\sigma/\sigma=(1/(X+\Delta X)-1/X)/(1/X)$$

$$=-\ X/(X+\Delta X)$$

$$=pP(Xt-Xs)/(Xs+3Xt) \qquad \text{(III.4)}$$

The important points to note are that the absolute value of the change in conductivity increases with increasing polarization and increasing spin dependence of the scattering cross section, and that $\Delta\sigma$ can be of either sign, depending on the sign of $(Xt-Xs)$.

Lepine and Prejean (3) reported spin-dependent photoconductivity in silicon in which the number of carriers was a function of the spin polarization of their recombination centers. Instead of triplet and singlet scattering cross-sections, one has triplet and singlet capture cross-sections, and thus a recombination rate depending on spin polarization. The recombination centers responsible were thought to be paramagnetic surface centers. Kurylev and Karyagin (4,5) observed spin-dependent recombination at surface sites in germanium.

Spin-dependent photoconductivity in plastically deformed silicon was investigated by two groups independently. Grazhulis etal (6) observed, in p-type deformed silicon at liquid helium temperatures, a resonant decrease in photoconductivity coincident with the spin resonance of the dislocation spin system. They attributed their results to the spin dependence of the scattering of free carriers by dislocations. Wosinski and Figielski (7) made a similar observation in n-type deformed silicon at temperatures between 80 and 340 K, but attributed their results to spin dependent recombination of free electrons at dislocations. Wosinski etal (8) describe a contactless method for measuring the spin dependent photoconductivity in which they monitor the change in Q of a cavity loaded with the sample. Their contactless method is exactly equivalent to electric detection of magnetic resonance. Since conventional EPR results were already available for the silicon dislocation spin system, both groups were able to make a direct comparison between their spin-dependent photoconductivity spectrum and the EPR spectrum. Spin-dependent increases in conductivity were observed by Szkielko (9) in dislocated silicon p-n junctions. He attributed his results to spin-dependent generation of carriers at dislocations.

The results of the spin-dependent photo-conductivity studies of dislocated silicon have a direct bearing on the work I have done on germanium. In particular, they were of considerable aid in the interpretation of the results to be presented in the following chapter.

CHAPTER IV - RESULTS AND THEORETICAL ANALYSIS

IV.1 - INTRODUCTION

This chapter contains the main body of experimental results, with the exception of those for the lithium-diffused crystals, which appear in CHAPTER V.

I have observed two new sets of EPR lines (1) in optically excited n-type germanium samples containing dislocations: 24 narrow lines (14 gauss peak-to-peak derivative width), and four broad lines (20 to 60 gauss peak-to-peak). Both spectra are associated with electrons at dislocations. The lines persist for hours after excitation and can be of either sign. When the magnetic field points along a <100> axis, all 28 lines converge to the simple spectrum centered at g=1.6 shown in Figure IV.1, adjacent to the arsenic donor hyperfine structure.

IV.2 - ANGULAR DEPENDENCE

As the magnetic field was rotated away from the <100> axis, the lines proved to be highly anisotropic.

Figure IV.2 is a plot of the angular dependence of the 24 narrow lines when the magnetic field was rotated approximately in the (110) plane. The spectrum consists of four main branches - two with six resolved lines each, and two branches which appear to have only three lines but actually become resolved into six when the magnetic field is rotated in a different plane. The overall symmetry of the four branches is that of the four <111> axes, so each <111> axis contributes six narrow lines. The two branches with six resolved lines each would have become superposed had the magnetic field been exactly in the (110) plane. The line intensities from each of the four <111> axes are in general not equal, the relative intensities being sample dependent.

When the magnetic field was rotated in the approximate (100) plane, the spectrum in Figure IV.3 was observed. Again, due to the slight misorientation, the contributions from the four <111> axes can be readily identified. Because the lower branch in the insert had an order of magnitude smaller signal than the upper branch, only four of the six lines were seen.

Misalignment was an aid in untangling the narrow lines, but near perfect alignment was needed to be able to track the broad lines over a large range of g values. The spectrum of broad lines appears in Figure IV.4. There is one line per <111> axis, but for perfect orientation in a

(100) plane there are two pair of equivalent <111> axes.

IV.3 - DETERMINATION OF THE g TENSORS

I found that all the data could be described using an effective spin Hamiltonian containing only the electronic Zeeman interaction term:

$$\mathcal{H} = \beta \vec{H} \cdot \overleftrightarrow{g} \cdot \vec{S} \quad . \qquad \text{(IV.1)}$$

Here β is the Bohr magneton, $\vec{H}$ the magnetic field, $\overleftrightarrow{g}$ the spectroscopic splitting tensor (due to orbital contributions, g is not in general isotropic.), and $\vec{S}$ the effective spin (defined so that the number of levels in the lowest group of states equals 2S+1). Recall (2) that the 2S+1 energy levels are given by

$$E(m_S) = \beta m_S H g \qquad \text{(IV.2)}$$

with

$$g = \mathrm{SQRT}(g_1^2 \cos^2(\theta_1) + g_2^2 \cos^2(\theta_2) + g_3^2 \cos^2(\theta_3)) \qquad \text{(IV.3)}$$

where the g_i are principal g values of the g tensor and θ_i are the angles H makes with the principal axes of the g tensor. m_S can assume all values from -S to +S at integer intervals, consequently the energy levels are equally spaced. A microwave field $\vec{H}_1 \cos(2\pi f t)$ is applied as a perturbation to induce transitions between these levels.

$$\mathcal{H}_1(t) = \mathcal{H}_1 \cos(2\pi f t) = \beta \vec{H}_1 \cdot \overleftrightarrow{g} \cdot \vec{S} \cos(2\pi f t) \qquad \text{(IV.4)}$$

A spin starting out in state m_s at t=0 has a probability, to first order in time dependent perturbation theory, of being in state m_s' at time t given by

$$p(m_s',t)=\hbar^{-2}\left|\int_0^t\langle\bar{m}_s|\mathcal{H}_1(t')|m_s'\rangle\exp(i(E(m_s)-E(m_s'))t'/\hbar)dt'\right|^2$$

$$=|\langle\bar{m}_s|\mathcal{H}_1|m_s'\rangle|^2\sin^2(t((E(m_s)-E(m_s'))/\hbar-2\pi f)/2)/((E(m_s)-E(m_s'))/\hbar-2\pi f)^2 \tag{IV.5}$$

Since the local field is not exactly the same for each spin, there is really a distribution of states peaked at $E(m_s)$ and $E(m_s')$. The transition probability per unit time averaged over the distribution of states is given by

$$w(m_s\rightarrow m_s')=G(f)\,|\langle\bar{m}_s|\mathcal{H}_1|m_s'\rangle|^2/(2\hbar)^2 \tag{IV.6}$$

where G(f) is a line shape function normalized so that $\int_0^\infty G(f)df=1$. Recall that in the anisotropic case m_s is no longer a projection of $\vec{S}$ along $\vec{H}$, but rather along an axis $\hat{z}$ with direction cosines

$$(g_1/g\cos\theta_1,\ g_2/g\cos\theta_2,\ g_3/g\cos\theta_3)$$

with respect to the principal axes of the g tensor. It will be the components of $\vec{H}_1$ normal to $\hat{z}$ which will generate a non-zero matrix element between states m_s and $m_s\pm 1$. When g is axially symmetric,

$$g(\theta_1)=\mathrm{SQRT}((g_\parallel^2-g_\perp^2)\cos^2(\theta_1)+g_\perp^2)\ , \tag{IV.7}$$

where θ_1 is the angle the magnetic field makes with the symmetry axis. A plot of g^2 against $\cos^2(\theta_1)$ then yields a straight line and the principal g values can be determined. Figure IV.5 is such a plot for the four broad lines where the symmetry axes are the four <111> axes. A least squares fit to a straight line yields

$g_{\parallel}=0.34$ and $g_{\perp}=1.94$.

This large anisotropy in g corresponds to a 41 kgauss spread in the spectrum at a frequency of 25 GHz.

The g tensor for the 24 narrow lines is arrived at in the same way. By inspection I found that the 24 line spectrum is identical to one resulting from spin 1/2 sites with the 24 symmetry axes,

$$\langle 111\rangle_i \pm \alpha\langle 110\rangle_k, \qquad \text{(IV.8)}$$

where i= 1 to 4 and k= 1 to 6, subject to the condition $\langle 111\rangle_i \cdot \langle 110\rangle_k=0$, with $\alpha=0.021$. The significance of α will be discussed in section IV.8. The principal g values, derived exactly as for the broad lines, are

$g_{\parallel}=0.73$ and $g_{\perp}=1.89$.

A comparison with g values for other defects in Ge appears in Table IV.1.

I used computer simulation of spectra to verify the identification of the symmetry axes. All simulations were made for the case of perfect crystal alignment. I chose a coordinate system with axes <100>, <010>, and <001>. For the first geometry, $\vec{H}$ is in the (110) plane and

$$\vec{H}=H\langle \sin(\theta)/\sqrt{2},\ -\sin(\theta)/\sqrt{2},\ \cos\theta \rangle$$

where θ is the angle $\vec{H}$ makes with respect to the <001> direction. There are six symmetry axes derived from the <111> axis. The unit vectors for these six axes are

$$\hat{1}_{[111]}=(\langle 111\rangle/\sqrt{3}+\alpha\langle 1\bar{1}0\rangle/\sqrt{2})/\mathrm{SQRT}(1+\alpha^2)$$

$$\hat{2}_{[111]}=(<111>/\sqrt{3}-\alpha<1\bar{1}0>/\sqrt{2})/SQRT(1+\alpha^2)$$

$$\hat{3}_{[111]}=(<111>/\sqrt{3}+\alpha<\bar{1}01>/\sqrt{2})/SQRT(1+\alpha^2)$$

$$\hat{4}_{[111]}=(<111>/\sqrt{3}-\alpha<\bar{1}01>/\sqrt{2})/SQRT(1+\alpha^2)$$

$$\hat{5}_{[111]}=(<111>/\sqrt{3}+\alpha<0\bar{1}1>/\sqrt{2})/SQRT(1+\alpha^2)$$

$$\hat{6}_{[111]}=(<111>/\sqrt{3}-\alpha<0\bar{1}1>/\sqrt{2})/SQRT(1+\alpha^2)$$

The cosine of the angle between $\vec{H}$ and each unit vector is

$$C_1=\cos(\vec{H},\hat{1})$$

$$=(\alpha\sin\theta+1/\sqrt{3}\cos\theta)/SQRT(1+\alpha^2)$$

$$C_2=\cos(\vec{H},\hat{2})$$

$$=(-\alpha\sin\theta+1/\sqrt{3}\cos\theta)/SQRT(1+\alpha^2)$$

$$C_3=\cos(\vec{H},\hat{3})$$

$$=(-\alpha/2\sin\theta+(1/\sqrt{3}+\alpha/\sqrt{2})\cos\theta)/SQRT(1+\alpha^2)$$

$$C_4=\cos(\vec{H},\hat{4})$$

$$=(\alpha/2\sin\theta+(1/\sqrt{3}-\alpha/\sqrt{2})\cos\theta)/SQRT(1+\alpha^2)$$

$$C_5=\cos(\vec{H},\hat{5})$$

$$=(\alpha/2\sin\theta+(1/\sqrt{3}+\alpha/\sqrt{2})\cos\theta)/SQRT(1+\alpha^2)$$

$$C_6=\cos(\vec{H},\hat{6})$$

$$=(-\alpha/2\sin\theta+(1/\sqrt{3}-\alpha/\sqrt{2})\cos\theta)/SQRT(1+\alpha^2)\ .$$

The six lines associated with the <111> direction are then calculated using the equation

$$g_k(\theta)=SQRT((g_\parallel^2-g_\perp^2)C_k^2+g_\perp^2)\ , \qquad (IV.9)$$

with k=1 to 6 and the experimentally determined principal g values. The six lines associated with the $<11\bar{1}>$ axis are identical to the ones just calculated.

Unit vectors for the six symmetry axes related to the $<\bar{1}11>$ direction are

$$\hat{1}_{[\bar{1}11]}=(1/\sqrt{3}\langle\bar{1}11\rangle+\alpha/\sqrt{2}\langle110\rangle)/SQRT(1+\alpha^{2})$$

$$\hat{2}_{[\bar{1}11]}=(1/\sqrt{3}\langle\bar{1}11\rangle-\alpha/\sqrt{2}\langle110\rangle)/SQRT(1+\alpha^{2})$$

$$\hat{3}_{[\bar{1}11]}=(1/\sqrt{3}\langle\bar{1}11\rangle+\alpha/\sqrt{2}\langle101\rangle)/SQRT(1+\alpha^{2})$$

$$\hat{4}_{[\bar{1}11]}=(1/\sqrt{3}\langle\bar{1}11\rangle-\alpha/\sqrt{2}\langle101\rangle)/SQRT(1+\alpha^{2})$$

$$\hat{5}_{[\bar{1}11]}=(1/\sqrt{3}\langle\bar{1}11\rangle+\alpha/\sqrt{2}\langle0\bar{1}1\rangle)/SQRT(1+\alpha^{2})$$

$$\hat{6}_{[\bar{1}11]}=(1/\sqrt{3}\langle\bar{1}11\rangle-\alpha/\sqrt{2}\langle0\bar{1}1\rangle)/SQRT(1+\alpha^{2})$$

The cosine of the angle between H and each unit vector is

$$C_1=(-2/\sqrt{6}\ \sin\theta+1/\sqrt{3}\ \cos\theta)/SQRT(1+\alpha^{2})$$

$$=C_2$$

$$C_3=(-2/\sqrt{6}\ \sin\theta+\alpha/2\ \sin\theta+1/\sqrt{3}\ \cos\theta+\alpha/\sqrt{2}\ \cos\theta)/SQRT(1+\alpha^{2})$$

$$=C_5$$

$$C_4=(-2/\sqrt{6}\ \sin\theta-\alpha/2\ \sin\theta+1/\sqrt{3}\ \cos\theta-\alpha/\sqrt{2}\ \cos\theta)/SQRT(1+\alpha^{2})$$

$$=C_6$$

The g values are again calculated using equation (IV.9).

The six unit vectors associated with the $\langle1\bar{1}1\rangle$ direction are

$$\hat{1}_{[1\bar{1}1]}=(1/\sqrt{3}\ \langle1\bar{1}1\rangle+\alpha/\sqrt{2}\ \langle110\rangle)/SQRT(1+\alpha^{2})$$

$$\hat{2}_{[1\bar{1}1]}=(1/\sqrt{3}\ \langle1\bar{1}1\rangle-\alpha/\sqrt{2}\ \langle110\rangle)/SQRT(1+\alpha^{2})$$

$$\hat{3}_{[1\bar{1}1]}=(1/\sqrt{3}\ \langle1\bar{1}1\rangle+\alpha/\sqrt{2}\ \langle011\rangle)/SQRT(1+\alpha^{2})$$

$$\hat{4}_{[1\bar{1}1]}=(1/\sqrt{3}\ \langle1\bar{1}1\rangle-\alpha/\sqrt{2}\ \langle011\rangle)/SQRT(1+\alpha^{2})$$

$$\hat{5}_{[1\bar{1}1]}=(1/\sqrt{3}\ \langle1\bar{1}1\rangle+\alpha/\sqrt{2}\ \langle\bar{1}01\rangle)/SQRT(1+\alpha^{2})$$

$$\hat{6}_{[1\bar{1}1]}=(1/\sqrt{3}\ \langle1\bar{1}1\rangle-\alpha/\sqrt{2}\ \langle\bar{1}01\rangle)/SQRT(1+\alpha^{2})$$

The cosine of the angle between H and each unit vector is

$$C_1=(2/\sqrt{6}\ \sin\theta+1/\sqrt{3}\ \cos\theta)/SQRT(1+\alpha^{2})$$

$$=C_2$$

$$C_3=(2/\sqrt{6}\ \sin\theta-\alpha/2\ \sin\theta+1/\sqrt{3}\ \cos\theta+\alpha/\sqrt{2}\ \cos\theta)/SQRT(1+\alpha^{2})$$

$=C_5$

$C_4=(2/\sqrt{6}\ \sin\theta+\alpha/2\ \sin\theta+1/\sqrt{3}\ \cos\theta-\alpha/\sqrt{2}\ \cos\theta)/\mathrm{SQRT}(1+\alpha^2)$

$=C_6$

The g values are again calculated using equation (IV.9). Figure IV.6 shows the simulated spectrum of the 24 narrow lines for the magnetic field in the (110) plane.

In the second geometry, the magnetic field is rotated in the (100) plane and

$\vec{H}=H\langle 0,\cos\theta,-\sin\theta\rangle$.

The cosine of the angle between H and each of the six axes derived from the <111> direction are

$C_1=(\cos\theta(1/\sqrt{3}-\alpha/\sqrt{2})-1/\sqrt{3}\ \sin\theta)/\mathrm{SQRT}(1+\alpha^2)$

$C_2=(\cos\theta(1/\sqrt{3}+\alpha/\sqrt{2})-1/\sqrt{3}\ \sin\theta)/\mathrm{SQRT}(1+\alpha^2)$

$C_3=(1/\sqrt{3}\ \cos\theta-\sin\theta(1/\sqrt{3}+\alpha/\sqrt{2}))/\mathrm{SQRT}(1+\alpha^2)$

$C_4=(1/\sqrt{3}\ \cos\theta-\sin\theta(1/\sqrt{3}-\alpha/\sqrt{2}))/\mathrm{SQRT}(1+\alpha^2)$

$C_5=(\cos\theta(1/\sqrt{3}-\alpha/\sqrt{2})-\sin\theta(1/\sqrt{3}+\alpha/\sqrt{2}))/\mathrm{SQRT}(1+\alpha^2)$

$C_6=(\cos\theta(1/\sqrt{3}+\alpha/\sqrt{2})-\sin\theta(1/\sqrt{3}-\alpha/\sqrt{2}))/\mathrm{SQRT}(1+\alpha^2)$

The expressions for the six axes derived from the $\langle\bar{1}11\rangle$ are identical to these.

The cosine of the angle between H and each of the six axes derived from the $\langle 1\bar{1}1\rangle$ direction are

$C_1=(\cos\theta(1/\sqrt{3}-\alpha/\sqrt{2})+1/\sqrt{3}\ \sin\theta)/\mathrm{SQRT}(1+\alpha^2)$

$C_2=(\cos\theta(1/\sqrt{3}+\alpha/\sqrt{2})+1/\sqrt{3}\ \sin\theta)/\mathrm{SQRT}(1+\alpha^2)$

$C_3=(1/\sqrt{3}\ \cos\theta-\sin\theta(\alpha/\sqrt{2}-1/\sqrt{3}))/\mathrm{SQRT}(1+\alpha^2)$

$C_4=(1/\sqrt{3}\ \cos\theta+\sin\theta(\alpha/\sqrt{2}+1/\sqrt{3}))/\mathrm{SQRT}(1+\alpha^2)$

$C_5=(\cos\theta(1/\sqrt{3}+\alpha/\sqrt{2})-\sin\theta(\alpha/\sqrt{2}-1/\sqrt{3}))/\mathrm{SQRT}(1+\alpha^2)$

$$C_6=(\cos\theta(1/\sqrt{3}-\alpha/\sqrt{2})+\sin\theta(\alpha/\sqrt{2}+1/\sqrt{3}))/\mathrm{SQRT}(1+\alpha^2)$$

Likewise for the $<11\bar{1}>$ direction. The g values are again calculated from equation (IV.9). Figure IV.7 shows the simulated spectrum when the magnetic field is rotated in the (100) plane.

IV.4 - DEPENDENCE ON OPTICAL EXCITATION

Neither the four line spectrum nor the 24-line spectrum was seen prior to illumination of the sample. Radiation from the 300° K window was sufficient to induce both spectra, but the effectiveness of this mode of excitation was sample dependent. Between 10 and 1000 % enhancement could be achieved with a mercury vapor arc lamp through a 2 mm thick room temperature Ge filter, the size of the enhancement being sample dependent. Typically, samples in which the window radiation was least effective underwent the largest enhancements. The intensity of the light had a pronounced effect on the shape of the lines. Figure IV.8 shows the effect of placing a 10 db neutral density filter in front of the lamp. The lines were absent during illumination with the totally unfiltered arc lamp, but were maximized after such illumination. Presumably, the holes created while pumping above the band gap combine with dangling bonds to cause extinction of the signal.

I first attempted to study the excitation spectrum by placing a spectrometer in front of the lamp. No conclusive results were obtained in this way, probably because the intensity of the light getting through the spectrometer was too small to make a substantial change in the signal. So instead of the spectrometer I used the set of long pass filters listed in Table II.1. Each long pass filter was used in conjunction with the Ge filter and the 20 db neutral density filter. The size of the arsenic hyperfine structure was monitored to check for any changes in coupling of the mode to the cavity. The results are shown in Figure IV.9. Enhancement sets in at a photon energy of about 600 meV.

IV.5 - EFFECT OF MICROWAVE POWER

Early in the study, analysis of the spectrum was hampered by the extreme asymmetry of the lines. The asymmetry could be decreased by decreasing the microwave power going into the cavity, but the lower limit of the apparatus was 0.5×10^{-6} watts. Installing additional attenuators along the waveguide had a pronounced effect on the shape of the lines. Figure IV.10 shows one of the broad lines at (a) 0.5×10^{-8} watts and at (b) 0.5×10^{-6} watts. At low power the ambiguity as to the sense of the line is eliminated. Figure IV.11 compares several of the narrow lines at (a) 0.5 X 10^{-8} watts and at (b) 0.5 X 10^{-7} watts. All samples showed qualitatively the same behavior, but due to variations from sample to sample a quantitative study was not attempted.

IV.6 - LIFETIME

Since optical excitation was required to induce the lines, it was of interest to study the decay of the spectrum after the removal of the excitation source. In general, the signal amplitude decreased during the first 20 minutes after closing the shutter and then levelled off. In one case I monitored the signal for three hours 50 minutes, and once it had levelled off it showed no signs of further decay. The percentage drop in the first 20 minutes was sample dependent but typically fell into the range 60 to 80 %. Time dependences for two samples at opposite ends of this range are plotted in Figure IV.12. I checked for the electron cyclotron resonance signal to make sure there were no light leaks. EPR of an equally long-lived photo induced excited state has been reported for dislocated Si (9).

IV.7 – RELATION TO DISLOCATIONS

This section will cover the collection of experimental evidence indicating that these two new spectra arise from electrons at dislocations. The first piece of evidence is the failure to observe the spectra in a dislocation-free sample. All the other characteristics (see Table II.2) of that sample were the same as for crystals which did give the new lines; in particular, I observed normal shallow donor hyperfine structure and cyclotron resonance signals.

Further evidence that the new spectra are tied to dislocations is the large discrepancy between the line intensities from each of the <111> axes, as mentioned in Section IV.2. This behavior is explicable for a distribution of spins on line defects, but not point defects. If the spins were distributed on isolated point defects, the <111> directions, being equivalent, would each have a probability 1/4 of being occupied, and one would see very nearly equal contributions from the four axes. In the case of dislocations, however, once they begin to nucleate in the plane perpendicular to a given axis, it would require energy to turn cut of that plane. The result is a preponderance of dislocations in one plane. The line intensity from one of the <111> axes was typically five to 10 times that of the others. The extreme case was the vacuum grown crystal, in which I observed a signal exclusively from one axis. Another interesting case was the <111> grown crystal, in which I observed no signal from the growth axis, i.e., no dislocations run perpendicular to the growth axis.

Additional evidence linking the new spectra to dislocations is the symmetry of the 24 line spectrum. The expression for the symmetry axes given in Section IV.3 specifically relates each <111> axis to the three <110> axes perpendicular to it. As mentioned in Chapter I, dislocation lines in the tetrahedral structure run along <110> directions, so the results are consistent with a model in which the signal is due to dislocation dangling bonds which are nearly perpendicular to the dislocation lines.

Yet another connection to dislocations is seen in the sign reversal of the lines in crystals grown in hydrogen and/or deuterium atmospheres. For normal EPR magnetic dipole absorption lines, as detected by the magnetic field of the cavity, sign reversal could result from spin population inversion created by spin dependent relaxation processes in the optical pumping cycle. This interpretation however cannot explain the persistence of the lines for hours after removal of optical pumping and after repeated passage through spin resonance. The signal reversal can be understood within the framework of spin dependent conductivity and electric detection of magnetic resonance. Figure IV.13 is a blowup of a dislocation line, showing schematically triplet and singlet scattering of two photo excited electrons by dangling bond electrons. As described in Chapter III, the relative magnitude of the singlet and triplet scattering cross sections determines the sign of the lines. According to this model, crystals grown in hydrogen and/or deuterium have a larger singlet scattering cross section, while the opposite is true for vacuum or argon grown crystals. Although this difference is most likely due to the presence of hydrogen at dislocations, the detailed mechanism by which the hydrogen changes the scattering cross section is not known at this time. The fact that the effect persists long after the decay of free carriers, as evidenced by the decay of the electron cyclotron resonance signal, suggests that some of the electrons may get trapped by dislocations and still retain some mobility along the dislocation lines (10). It is these mobile electrons which may be giving rise to the four line spectrum, although the possibility that a different scattering center is responsible has not been ruled out.

One may argue that not a single piece of evidence presented thus far is very conclusive as to the origin of the lines. When taken together, however, they build a convincing argument for the interpretation that the spectra are the electrically detected magnetic resonance of electrons at dislocations. The next step is to try to deduce from the results something about the microscopic structure of the dislocations.

IV.8 - DISTORTION OF THE DISLOCATION DANGLING BONDS

Returning to expression IV.8 for the symmetry axes of the dislocation dangling bond spectrum, the quantity α is a measure of the deviation of the axes away from a <111> direction. Figure IV.14 shows the six possible tilt directions associated with the <111> axis. Since the anisotropy of the g-tensor results from the anisotropy of the orbital contribution to g, the g-tensor symmetry axis coincides with the dislocation dangling bond axis. Let δ be the angle between the dislocation dangling bond and the <111> direction. Then

$$\cos\delta = 1/\sqrt{3}\ \langle 111\rangle\cdot(1/\sqrt{3}\,\langle 111\rangle+.021/\sqrt{2}\ \langle 1\bar{1}0\rangle)/\mathrm{SQRT}(1+.021^2) \qquad (\mathrm{IV.10})$$

or $\delta = 1.2^\circ$

The 1.2° tilt of the dislocation dangling bonds could be an intrinsic distortion characteristic of the dislocation or it could be the result of a Peierls-like instability. In the case of intrinsic distortion, there are several geometries, shown in Figure IV.15, consistent with the data: (a) All dangling bonds in a given dislocation are tilted in the same direction, and along the dislocation line. (b) The dangling bonds are tilted alternately in opposite directions along the dislocation line. (c) The dislocation dangling bonds are tilted in the direction of the Burgers vector. In principle, one could test for this possibility by selectively inducing dislocations in one direction and then observing the tilt direction in the EPR g-tensor axis.

The distortion shown in Figure IV.15(b) could alternatively arise from an instability with respect to dimerization of a linear chain of charges and/or spins. Peierls (11) considered the problem of a linear chain of atoms with lattice spacing "a" and one electron per site. The electrons fill one half the energy band shown in Figure IV.16(a). Distorting the potential slightly by dimerizing the chain, ie increasing the lattice spacing to "2a", halves the basic cell in reciprocal space. The distorted potential opens a gap in the energy band resulting in the two bands in Figure IV.16(b). Treating the distortion as a perturbation yields for the size of the gap

$$V(\pi/2a) = \langle \Psi(\pi/2a) | \delta V | \Psi(-\pi/2a) \rangle \qquad \text{(IV.11)}$$

where δV is the change in potential caused by the distortion and the Ψ are the wave functions for the undistorted chain. The effect of the gap is to lower the energy of some of the states in the lower band, and to raise the energy of some of the states in the upper band, the mean value remaining unchanged. Since only the lower band is occupied, however, there is a net reduction in energy and this is what drives the instability.

A completely analogous situation arises when one considers a linear chain of spins coupled by nearest neighbor antiferromagnetic exchange. In this spin-Peierls transition (12) the uniform antiferromagnet is unstable with respect to spin lattice dimerization into an alternating antiferromagnet. Pincus (13) has shown this explicitly for the X - Y model of antiferromagnetic exchange. Such a dimerization would again result in the distortion shown in Figure IV.15(b).

It is unclear at this time which, if any, of these Peierls transitions is taking place along the dislocations in Ge. Grazhulis, Kveder, and Osipyan (14) observed a dramatic drop in the magnetic susceptibility of the dislocation spin system in silicon at T=50 K. They interpreted this drop as being due to an instability with respect to the pairing of neighboring dangling bonds to form singlet pairs (S=0). Unfortunately, the use of the Ge sample as a high Q cavity precludes such a temperature dependence study in my case.

The results described thus far are totally different from those observed for the lithium diffused crystals, which I will present next.

CHAPTER V - LITHIUM AT DISLOCATIONS IN Ge

The behavior of lithium in Ge is of both technological and fundamental interest and has been studied in some detail (1 - 5). Lithium is a shallow donor, and as an interstitial impurity, it diffuses rapidly, but can also be trapped at defects to form shallow donor complexes (for example, LiO). Reiss et al (1) postulate ion pairing between lithium ions and acceptor sites in dislocations. Clearly if the lithium were to bind to the dislocation dangling bonds, one would no longer expect to see the dangling bond EPR spectrum described in Chapter IV. When studying a lithium diffused Ge crystal containing dislocations, I did in fact observe a totally different spectrum, arising from lithium at dislocations.

Two samples, one dislocation free cut from boule S - 29 and one containing dislocations ($\sim 10^3$ cm^{-2}) cut from boule 370, were first saturated with lithium by diffusion from the surface at 400° C. The lithium was then out diffused for several days at 200° C until a net donor concentration $\lesssim 10^{13}$ cm^{-3} was achieved. After the out diffusion, virtually all the free lithium has left the crystal and one is left with lithium bound at defects.

Crystals grown from quartz crucibles have oxygen concentrations $\sim 10^{14}$ cm^{-3} and some of the lithium is present in the form of the LiO complex. This complex gives rise to an EPR spectrum (5) with an axially symmetric g - tensor, about the four <111> axes. The principal g values are $g_{\parallel}=0.85$ and $g_{\perp}=1.91$. This four line spectrum is the only lithium related spectrum observed in the lithium diffused dislocation free sample.

The dislocated sample had an additional spectrum superimposed on the four line LiO spectrum. The angular dependence of the combined spectrum appears in Figure V.1. The large number of closely spaced lines (not resolved for all angles) together with imperfect crystal orientation made analysis of the spectrum difficult. I deduced the principal g values as follows. I used computer simulation (see Appendix) to reproduce the main features of the spectrum. In particular, the parts of the spectrum near g=1.9 have near zero slope and so are practically unaffected by slight sample misorientation. Those parts were fitted quite well by taking for principal axes $\langle 110 \rangle$, $\langle 1\bar{1}\bar{2} \rangle$, and $\langle 1\bar{1}1 \rangle$ (plus equivalent sets) and superposing the LiO spectrum. This corresponds to one axis along a dangling bond (due to the presence of lithium, it is not really a dangling bond any more), one axis along a dislocation perpendicular to the dangling bond, and the third axis perpendicular to the other two. The principal g values are 1.917 ± 0.002, 1.896 ± 0.002, and 0.855 ± 0.010 respectively. This g tensor very accurately reproduces the upward displacement of the lines at 35° with respect to the lines at 90°. After the displacement, the lowest dislocation line at 35° can no longer be resolved from the LiO line so that only two lines are seen as opposed to three at 90°. The presence of the LiO spectrum leads to some ambiguity about whether or not there is a tilt of the dangling bond axis. The splittings caused by such a tilt could easily be camouflaged by the LiO lines. If there is a tilt, it would have to be $\lesssim 0.3°$. The lithium has apparently suppressed the distortion and has resulted instead in the 1% nonaxiallity of the g tensor. To obtain a higher degree of accuracy in g tensor determination one could repeat these experiments on a spectrometer operating in a higher band of frequencies.

The question arises as to whether or not the lines associated with the lithium at dislocations have been electrically detected. Had they been reversed in sign the answer would have been clear, but they were not reversed. Also, optical pumping was not required to induce the spectrum. In spite of these facts, there are still some indications that electric detection may be involved.

Consider a model in which positive lithium ions are located at dangling bond sites. In the neutral configuration each ion has a shallowly bound electron in some roughly hydrogenic orbit. Rather than being scattered throughout the bulk, these donors are lined up along the dislocations resulting in considerable overlap of the donor electron wave function and consequently a conducting path along the dislocations, with the conductivity again being spin dependent.

The evidence supporting this model is the observation of an electron cyclotron resonance signal for the optically shielded dislocated crystal comparable to that for the optically pumped dislocation free crystal. The shallow donor electrons are evidently being accelerated along dislocations by the microwave electric field until impact ionization into the conduction band takes place. This can also explain why I did not observe any broad lines from the spin resonance of the mobile electrons. Above band gap light does not destroy the dislocation – lithium spectrum as it does the dislocation dangling bond spectrum. In the latter case, the dangling bonds are presumable consumed by holes, whereas in the former case the positive charge of the lithium ions repels holes thus preventing the annihilation of the dangling bonds.

To summarize, I have compared the spectrum of a lithium diffused dislocated Ge crystal to those of a lithium diffused dislocation free crystal and an ultra pure dislocated crystal. Due to the absence of the dislocation dangling bond spectrum in the dislocated crystal containing lithium, and the presence of a new spectrum which is absent in the dislocation free crystal, it is reasonable to conclude that lithium ions very likely become bound at dangling bond sites. Electrons are so shallowly bound to these ions that they are easily promoted by the microwaves into the conduction band, resulting in a strong electron cyclotron resonance signal in the absence of optical pumping.

CHAPTER VI - SUMMARY AND CONCLUSIONS

Using the ultrasensitive techniques of high Q self resonant samples and electric detection of magnetic resonance, I have been able to study Ge crystals of low dislocation densities. This has the advantage of allowing me to look only at dislocations formed during crystal growth, ie those which can be considered "naturally occurring". When studying dislocations created via plastic deformation, one has always to wonder how their properties compare to those of the naturally occurring varieties. This question does not arise in the present work.

To summarize the results of the study, I will begin by remarking that I saw no paramagnetism in the ground state (ie in the absence of optical excitation). There are two equally acceptable explanations for this. The first is that the spins are all paired, leaving an S=0 configuration. The second is that the spins are so few in number that they can only be electrically detected, this requiring the prior introduction of current carriers.

I did observe paramagnetic centers in optically excited crystals. Some of these centers had the symmetry of the dislocation dangling bonds, with a six-fold 1.2° distortion. The others had the symmetry of the <111> crystal axes, and may be photoexcited electrons conducting along dislocations. I saw no evidence of the superparamagnetism (strings of spins coupled to form S > 1/2 species) reported by Schmidt, Weber, Alexander, and Sander (1) for dislocated Si.

I used electric detection to observe the spin resonances. This was possible only because of the spin dependent conductivity of the photoexcited carriers. I observed this spin dependent conductivity to persist for hours after the removal of excitation.

Finally, I showed that the same techniques could be used to study the interaction of impurities with dislocations. Specifically, I found that lithium diffused into a crystal led to an entirely new dislocation spectrum. This suggests that the lithium is located at dangling bond sites. Also, the presence of the bulk LiO spectrum opens up the possibility of studying the comparative rates of bulk and dislocation diffusion.

The results presented in this thesis illustrate the power of the EPR technique in the study of semiconductors. Not only can it provide us with microscopic structural information, but when coupled with electric detection, it can also tell us something about charge transport within the crystal.

EPILOGUE

I will take this opportunity to give the reader an historical view of this research. Professor Jeffries had the idea to try to observe the effect excitons bound to shallow donors would have on the shallow donor hyperfine structure. I tried very hard to observe an effect, in both silicon and germanium. My attempts were unsuccessful, possibly due to the short exciton lifetime.

It was during one of these attempts, however, that I decided to investigate a blur of nondescript wiggles in the spectrum downfield from the shallow donor hyperfine structure. These ultimately became the subject of this thesis. I found that when operating at the lowest possible microwave power some fairly symmetric lines emerged and the signal to noise ratio improved considerably. It was then that I noticed the reversed sign of the lines. It also became clear that there was a large number of lines - the harder I tried, the more lines I saw. Finally I had a plot of the entire angular distribution of 28 lines, for two different sample orientations. Then I was faced with the task of determining the origin of the lines and the form of the spin Hamiltonian. A long string of sample dependence studies ultimately zeroed in on the role of dislocations and the corresponding g - tensor. The final hurdle was to figure out the excitation/decay properties of the lines and their sign reversal. The relevant clues surfaced in the papers on spin dependent photo conductivity in silicon.

One final remark...I did attempt electron nuclear double resonance in germanium, with no success. The attempts were made without the benefit of a signal averager, however, so this problem may merit further study.

APPENDIX

I have listed here one entire computer program to illustrate how I produced computer simulations of the EPR spectra. This program was written to run on UC Berkeley's UNIX Basic - Plus in conjunction with a DTC 302 printer/terminal. It is designed to calculate and plot g as a function of magnetic field direction for the field in either the (100) or (110) plane, when given the principal g values g_1 , g_2 , and g_3 . The principal axes of the g tensor built into this program are $\hat{g}_1 \parallel \langle 111 \rangle$ (or equivalent), $\hat{g}_2 \parallel \langle 1\bar{1}0 \rangle$ or $\langle 10\bar{1} \rangle$ or $\langle 01\bar{1} \rangle$ (ie any of the three dislocation lines in the (111) plane), and $\hat{g}_3$ perpendicular to $\hat{g}_1$ and $\hat{g}_2$. Also built into this program is the option to tilt $\hat{g}_1$ away from <111> in the direction of the dislocation lines. The amount of tilt is variable and is specified by the parameter v1 through the relation

$$\cos(\text{tilt angle})=1/\text{SQRT}(1+\text{v1}^2)$$

where v1 corresponds to alpha in the text. The tilt can be thought of as a rotation of $\hat{g}_1$ and $\hat{g}_2$ about $\hat{g}_3$ by the tilt angle.

To use the program one must first create the following input file:

```
n1,s1,s2,h1,h,v1,v,f1,f2
i1,i2,i3
x0,x1,y0,y1
g1,g2,g3
c$(j8), n2, c1$(j8)
```

Explanation of line one:

n1= number of data sets to be plotted (ie number of nondegenerate <111> axes)

s1= width of plot in units of 25 cm

s2= height of plot in units of 88 cm

h1= increment of horizontal variable (degrees)

h= distance between horizontal tickmarks

v1= alpha

v= distance between vertical tickmarks

f1= 1

f2= 1

Explanation of line two:

i1= 0

i2= 0

i3= 0 for (100) plane, 1 for (110) plane

Explanation of line three:

x0= smallest value of horizontal variable

x1= largest value of horizontal variable

y0= smallest value of vertical variable

y1= largest value of vertical variable

Explanation of line four:

g1= principal g value for axis $\hat{g}_1$

g2= principal g value for axis $\hat{g}_2$

g3= principal g value for axis $\hat{g}_3$

Explanation of line five through line 4+n1:

c$(j8)= "." for plot character .

n2= number of points in branch j8

c1$(j8)= "g values:"

j8 ranges from 1 to n1 in integral steps.

One also needs a Plot file, which is also listed. This Plot file can be made executable via the command "chmod +x Plot". Then to run the program one just types "Plot Input" where Input is just the name of the input file. The program listing follows.

```
cat plot3.bas
10  ! - general plotting routine
15 rem plots based on 3 principal g values
20  dim x(277,1),y(277,1),c$(3)
22 def fnr(x)=int(x)+int(2*(x-int(x)))
25  print chr$(27);"A";chr$(27);"@";
30   open "zwork1" for input as file 1
40   input #1,n1,s1,s2,h1,h,v1,v,g1,g2
50  w1=1/sqr(1+v1**2)
52 w2=v1/sqr(2)
54 w3=v1*w1/sqr(3)
60 s1=590*s1 :s2=1663*s2
80   input #1,i1,i2,i3
90 if i3=0 then  r=(45+h1)/n1 else r=(90+h1)/n1
100  input #1,x0,x1,y0,y1
110 input #1,g7,g8,g9 !g7 is g parallel
122  gosub 3000   ! - to tickmarks
124  shell "stty nl" !  - alters return & linefeed
126  gosub 4000   ! - to axes
130 for j8=1 to n1
140  gosub 1000   ! - to data input
170 next j8
175  close 1
180  shell "stty -nl"   ! - unalters return & linefeed
190  print chr$(10);chr$(10);
200  print "horiz-axis tickmarks ";h;" apart, from ";x5;" to ";x6
210  print "vert-axis tickmarks ";v;" apart, from ";y5;" to ";y6
215 print "alpha=";v1
216 if i3=1 then print "(110)"
217 if i3=0 then print "(100)"
220  for j=1 to n1
230 print c1$(j);g7;g8;g9
240  next j
400  print chr$(27);"A";
500  goto 6000
1000 ! -  data input subroutine
1010  def ins(x)=sin(x*pi/180)
1020  def inc(x)=cos(x*pi/180)
1140  input #1,c$(j8),n2,c1$(j8)
1145  print chr$(27);"C";c$(j8);chr$(27);"B";
1150  ! - inputs plot character, #data pts.
1199 go to 1300
1200 if j8=2 then 1250
1204 i=i+1
1205 y(i,1)=sqr((g7*w1*(inc(x(i,1))*(1/sqr(3)-v1/sqr(2))-
ins(x(i,1))/sqr(2)))**2+(g8*(ins(x(i,1))*w3-inc(x(i,1))*(w2+w3)))**2_
+(g9*(inc(x(i,1))+2*ins(x(i,1)))/sqr(6))**2)
```

```
1209 i=2+k
1210 y(i,1)=sqr((g7*w1*(fnc(x(i,1))*(1/sqr(3)+v1/sqr(2))-
fns(x(i,1))/sqr(3)))**2+(g8*(fnc(x(i,1))*(w3-w2)-fns(x(i,1))*w3))**2_
+(g9*(fnc(x(i,1))+2*fns(x(i,1)))/sqr(6))**2)
1214 i=3+k
1215 y(i,1)=sqr((g7*w1*(fnc(x(i,1))/sqr(3)-fns(x(i,1))*(1/sqr(3)+
v1/sqr(2))))**2+(g8*(fns(x(i,1))*w2+w3*(fnc(x(i,1))-fns(x(i,1)))))**2_
+(g9*(2*fnc(x(i,1))+fns(x(i,1)))/sqr(6))**2)
1219 i=4+k
1220 y(i,1)=sqr((g7*w1*(fnc(x(i,1))/sqr(3)-fns(x(i,1))*(1/sqr(3)-
v1/sqr(2))))**2+(g8*(w3*(fnc(x(i,1))-fns(x(i,1)))-w2*fns(x(i,1))))**2_
+(g9*(2*fnc(x(i,1))+fns(x(i,1)))/sqr(6))**2)
1224 i=5+k
1225 y(i,1)=sqr((g7*w1*(fnc(x(i,1))*(1/sqr(3)-v1/sqr(2))-
fns(x(i,1))*(1/sqr(3)+v1/sqr(2))))**2+(g8*(fnc(x(i,1))*(w2+w3)+
fns(x(i,1))*(w2-w3)))**2_
+(g9*(fnc(x(i,1))-fns(x(i,1)))/sqr(6))**2)
1229 i=6+k
1230 y(i,1)=sqr((g7*w1*(fnc(x(i,1))*(1/sqr(3)+v1/sqr(2))-_
fns(x(i,1))*(1/sqr(3)-v1/sqr(2))))**2+(g8*(fnc(x(i,1))*(w3-w2)-_
fns(x(i,1))*(w2+w3)))**2_
+(g9*(fnc(x(i,1))-fns(x(i,1)))/sqr(6))**2)
1235 go to 1580
1250 i=1+k
1251 y(i,1)=sqr((g7*w1*(fnc(x(i,1))*(1/sqr(3)-v1/sqr(2))+
fns(x(i,1))/sqr(3)))**2+(g8*(fnc(x(i,1))*(-w2-w3)-fns(x(i,1))*w3))**2_
+(g9*(fnc(x(i,1))-2*fns(x(i,1)))/sqr(6))**2)
1255 i=2+k
1256 y(i,1)=sqr((g7*w1*(fnc(x(i,1))*(1/sqr(3)+v1/sqr(2))+
fns(x(i,1))/sqr(3)))**2+(g8*(fnc(x(i,1))*(w3-w2)+fns(x(i,1))*w3))**2_
+(g9*(fnc(x(i,1))-2*fns(x(i,1)))/sqr(6))**2)
1260 i=3+k
1261 y(i,1)=sqr((g7*w1*(fnc(x(i,1))/sqr(3)+fns(x(i,1))*(1/sqr(3)-
v1/sqr(2))))**2+(g8*(w3*fnc(x(i,1))+fns(x(i,1))*(w2+w3)))**2_
+(g9*(fns(x(i,1))-2*fnc(x(i,1)))/sqr(6))**2)
1265 i=4+k
1266 y(i,1)=sqr((g7*w1*(fnc(x(i,1))/sqr(3)+fns(x(i,1))*(1/sqr(3)+
v1/sqr(2))))**2+(g8*(w3*fnc(x(i,1))+fns(x(i,1))*(w3-w2)))**2_
+(g9*(fns(x(i,1))-2*fnc(x(i,1)))/sqr(6))**2)
1270 i=5+k
1271 y(i,1)=sqr((g7*w1*(fnc(x(i,1))*(1/sqr(3)+v1/sqr(2))+
fns(x(i,1))*(1/sqr(3)-v1/sqr(2))))**2+(g8*(fnc(x(i,1))*(w2-w3)-
fns(x(i,1))*(w2+w3)))**2_
+(g9*(fnc(x(i,1))+fns(x(i,1)))/sqr(6))**2)
1275 i=6+k
```

```
1270 y(i,1)=sqr((g7*w1*(fnc(x(i,1))*(1/sqr(3)-v1/sqr(2))+
fns(x(i,1))*(1/sqr(3)+v1/sqr(2))))**2+(g8*(fnc(x(i,1))*(w2+w3)+
fns(x(i,1))*(w3-w2)))**2_
+(g9*(fnc(x(i,1))+fns(x(i,1)))/sqr(6))**2)
1280 go to 1580
1300  ! - determines x
1301  if i1=1 then 1400
1320  for i=1 to n2
1325 ft=(i-1)*r/n2
1330 x(i,1)=ft*n1
1340  next i
1399  goto 1500
1400  ! - inputs x
1500  if i2=1 then 1600
1501  ! - determines y
1502 l=n2/r
1503 n=n2-l
1505 for k=0 to n step 1
1506 if i3=0 then 1200
1510 if j8=2 go to 1534
1515 if j8=3 go to 1549
1519 i=1+k
1520 y(i,1)=sqr((g7*w1*(fnc(x(i,1))/sqr(3)-2*fns(x(i,1))/sqr(6)))**2+
(g8*w3*(2*fns(x(i,1))/sqr(2)-fnc(x(i,1)))))**2_
+(g9*(fns(x(i,1))/sqr(2)+fnc(x(i,1)))*2/sqr(6))**2)
1524 i=2+k
1525 y(i,1)=sqr((g7*w1*(fns(x(i,1))*(v1/2-2/sqr(6))+
fnc(x(i,1))*(v1/sqr(2)+1/sqr(3))))**2+(g8*(fnc(x(i,1))*(w2-w3)+
fns(x(i,1))/sqr(2)*(w2+2*w3)))**2_
+(g9*(fns(x(i,1))/sqr(2)+fnc(x(i,1)))/sqr(6))**2)
1529 i=3+k
1530 y(i,1)=sqr((g7*w1*(fnc(x(i,1))*(1/sqr(3)-v1/sqr(2))-
fns(x(i,1))*(2/sqr(6)+v1/2)))**2+(g8*(fnc(x(i,1))*(w2+w3)+
fns(x(i,1))*(w2-2*w3)/sqr(2)))**2_
+(g9*(fns(x(i,1))/sqr(2)+fnc(x(i,1)))/sqr(6))**2)
1531 go to 1580
1534 i=1+k
1535 y(i,1)=sqr((g7*w1*(2/sqr(6)*fns(x(i,1))+fnc(x(i,1))/sqr(3)))**2+
(g8*w3*(2*fns(x(i,1))/sqr(2)+fnc(x(i,1)))))**2_
+(g9*(fns(x(i,1))/sqr(2)-fnc(x(i,1)))*2/sqr(6))**2)
1539 i=2+k
1540 y(i,1)=sqr((g7*w1*(fns(x(i,1))*(2/sqr(6)-v1/2)+
fnc(x(i,1))*(1/sqr(3)+v1/sqr(2))))**2+(g8*(fnc(x(i,1))*(w2-w3)-
fns(x(i,1))/sqr(2)*(w2+2*w3)))**2_
+(g9*(fns(x(i,1))/sqr(2)-fnc(x(i,1)))/sqr(6))**2)
1544 i=3+k
```

```
1545 y(i,1)=sqr((g7*w1*(fns(x(i,1))*(2/sqr(6)+v1/2)+
fnc(x(i,1))*(1/sqr(3)-v1/sqr(2))))**2+(g8*(fnc(x(i,1))*(w2+w3)+
fns(x(i,1))*(2*w3-w2)/sqr(2)))**2_
+(g9*(fnc(x(i,1))-fns(x(i,1))/sqr(2))/sqr(6))**2)
1546 go to 1580
1549 i=1+k
1550 y(i,1)=sqr((g7*w1*(v1*fns(x(i,1))+fnc(x(i,1))/sqr(3)))**2+
(g8*(w2*2*fns(x(i,1))/sqr(2)-w3*fnc(x(i,1)))))**2_
+(g9*2*fnc(x(i,1))/sqr(6))**2)
1554 i=2+k
1555 y(i,1)=sqr((g7*w1*(fnc(x(i,1))/sqr(3)-v1*fns(x(i.1)))))**2+
(g8*(w2*2*fns(x(i,1))/sqr(2)+w3*fnc(x(i;1)))))**2_
+(g9*2*fnc(x(i,1))/sqr(6))**2)
1559 i=3+k
1560 y(i,1)=sqr((g7*w1*(fnc(x(i,1))*(1/sqr(3)+v1/sqr(2))-
v1/2*fns(x(i,1)))))**2+(g8*(fnc(x(i,1))*(w2-w3)-
fns(x(i,1))*w2/sqr(2)))**2_
+(g9*(sqr(3)*fns(x(i,1))/2+fnc(x(i,1))/sqr(6)))**2)
1564 i=4+k
1565 y(i,1)=sqr((g7*w1*(v1/2*fns(x(i,1))+fnc(x(i,1))*(1/sqr(3)-
v1/sqr(2)))))**2+(g8*(fnc(x(i.1))*(w2+w3)-fns(x(i,1))*w2/sqr(2)))**2_
+(g9*(sqr(3)*fns(x(i,1))/2+fnc(x(i.1))/sqr(6)))**2)
1569 i=5+k
1570 y(i,1)=sqr((g7*w1*(v1/2*fns(x(i,1))+fnc(x(i,1))*(1/sqr(3)+
v1/sqr(2)))))**2+(g8*(fnc(x(i,1))*(w2-w3)+fns(x(i,1))*w2/sqr(2)))**2_
+(g9*(fnc(x(i,1))/sqr(6)-sqr(3)*fns(x(i,1))/2))**2)
1574 i=6+k
1575 y(i,1)=sqr((g7*w1*(fnc(x(i,1))*(1/sqr(3)-
v1/sqr(2))-v1/2*fns(x(i,1)))))**2+(g8*(fnc(x(i,1))*(w2+w3)+
w2*fns(x(i,1))/sqr(2)))**2_
+(g9*(fnc(x(i,1))/sqr6)-sqr(3)*fns(x(i,1))/2))**2)
158 for j=1+k to n2/r+k
1582 (j,1)=fnr((xj,1)-x0)/(x-x0)*s1)
y(j,1)=fnr((y(j,1)-y0)/(yy0*s2)
1585 gosub 5000
1590 next
1595 shell "sleep 1"
1596 next k
1599  go  1700
1600  ! -  inputs y
1700  print chr$(27);
1800  return
3000rem - compute tikmarks
3010 k1=int(x1/h)+int(-x0/h)+1
3040  for i=1 to k1
3050  x(i,1)=fnr(((-int(-x0/h)+i-1)*h-x0)*s1/(x1-x0))
3060  next i
```

```
3065  x5=-int(-x0/h)*h:x6=x5+(k1-1)*h
3170  k2=int(y1/v)+int(-y0/v)+1
3180  for i=1 to k2
3190  y(i,0)=int(((-int(-y0/v)+i-1)*v-y0)*s2/(y1-y0))
3200  next i
3205  y5=-int(-y0/v)*v:y6=y5+(k2-1)*v
3300  return
4000 rem axes subroutine
4020  print chr$(13);chr$(6);
4025  rem - vertical axis
4030  j=k2:y(k2+1,0)=s2:y(0,0)=0
4040  if y(k2,0)=y1-y0 then 4110
4050  d=y(j+1,0)-y(j,0)
4060  if d=0 then 4100
4070  for i=1 to d
4080  print ".";chr$(10);
4090  next i
4100  if y(j,0)=0 then 4170
4110  for i=1 to 15
4120  print " .";
4130  next i
4140  print chr$(13);
4150  j=j-1
4160  goto 4050
4165  rem - horiz. axis
4170  x(0,0)=0:x(k1+1,0)=s1
4180  if x(1,0)=0 then j=1 else j=0
4190  d=x(j+1,0)-x(j,0)
4200  if d=0 then 4240
4210  for i=1 to d
4220  print " .";
4230  next i
4240  if j>=k1 then 4350
4250  for i=1 to 12
4260  print chr$(26);".";
4270  next i
4280  for i=1 to 12
4300  print chr$(10);
4310  next i
4320  j=j+1
4330  if j>k1 then 4240
4340  goto 4190
4350  print chr$(27);chr$(6);chr$(13);
4360  return
5000 ! - super plot subroutine
5010  j2=j
5020  x(0,1)=0:y(0,1)=0:x(n2+1,1)=0:y(n2+1,1)=0
```

```
5050  d1=x(j2,1)-x(j2-1,1):a1=abs(d1)
5060  d2=y(j2,1)-y(j2-1,1):a2=abs(d2)
5070  a=53.5-sgn(d2-.1)/2-sgn(d1-.1)
5080  p1=0:p2=0     ! - p1=p2=1 on last move
5090  if a1<=7 then p1=1
5100  if a2<=7 then p2=1
5110  m1=(a1-7)*p1+7:m2=(a2-7)*p2+7
5120  a1=a1-m1:a2=a2-m2
5130  f=1-int((j2+.1)/(n2+1))    ! - f=0 if j2=n2+1  f=1 otherwise
5140  print chr$(a-4*p1*p2*f);chr$(64+8*m1+m2);
5150  if p1+p2<1.5 then 5050
5160 if j2=n2 then j2=n2+1:go to 5050
5150  return
6000 end
.

  cat plot
cat $1>zwork1
basic+<<'mark'
run plot
bye
'mark
.
```

ACKNOWLEDGEMENTS

I am especially grateful to Professor Carson D. Jeffries - whose artistry and experimental wizardry have been a constant inspiration to me - not only for his expert guidance over the course of this work, but also for having had enough faith in me to let me join his research group after a seven year absence from physics.

I would like to thank William L. Hansen and Professor Eugene E. Haller for supplying me with a variety of Ge crystals, and the Semiconductor Materials and Devices Group at Lawrence Berkeley Laboratory for the use of their sample preparation facilities. I would particularly like to thank Professor Haller for preparing the lithium diffused samples, and for sharing with me his wealth of knowledge on the physics of Ge.

I am grateful to my thesis committee, Profs. Carson D. Jeffries, Alan M. Portis, and Eugene E. Haller, for their careful reading of my thesis and for their comments and suggestions.

I would also like to thank Professor Sumner P. Davis for many helpful discussions and moral support, James C. Culbertson for help with the plot routine, and Gloria Pelatowski for her speed and accuracy in preparing the figures.

I am grateful to the National Science Foundation for supporting me financially during my first three years of graduate study, and to the Materials Sciences Division of the U. S. Department of Energy.for supporting this research.

FOOTNOTES TO CHAPTER I

1 Readers unfamiliar with this technique are referred to Charles P. Poole, Jr., ELECTRON SPIN RESONANCE (Interscience Publishers, 1967) and to A. Abragam and B. Bleaney, ELECTRON PARAMAGNETIC RESONANCE OF TRANSITION IONS *(Clarendon Press, Oxford, 1970).*

2 James W. Corbett, Richard L. Kleinhenz, and Neal D. Wilsey, "Electron Paramagnetic Resonance in Semiconductors" in Materials Research Society Symposia Proceedings Volume 2, Defects in Semiconductors (North-Holland, 1981).

3 D. K. Wilson, Phys. Rev. 134, A265-A286 (1964).

4 DISLOCATIONS IN SOLIDS, Volume 5, edited by F. R. N. Nabarro (North-Holland, 1980).

5 See, for example, Journal de Physique, Colloque No. 6, Supplement C-6, (1979).

6 H. Alexander, R. Labusch, and W. Sander, Solid State Commun. 3, 357 (1965) <in German>.

7 J. Hornstra, J. Phys. Chem. Solids 5, 129 (1958).

FOOTNOTES TO CHAPTER II

1 J. P. Wolfe, PhD thesis, Physics Department, University of Californis, Berkeley, Ca (1971), unpublished.

2 For a detailed analysis of a high-Q microwave resonant sample see A. Okaya and L. F. Barasch, Proc. IRE 50, 2081 (1962). Our apparatus was designed for high Q TiO_2 resonant samples; its first use with high Q resonant Ge samples was by E. E. Haller and L. M. Falicov, Phys. Rev. Lett. 41, 1192 (1978) and E. E. Haller, W. L. Hansen, and F. S. Goulding, Adv. Phys. 30, 93 (1981), who found large signal enhancements.

FOOTNOTES TO CHAPTER III

1 B. C. Cavenett, Adv. Phys. 30, 475 (1981).

2 A. Honig, Phys. Rev. Lett. 17, 186 (1966).

3 D. J. Lepine and J. J. Prejean, Proceedings of the 10th International Conference on the Physics of Semiconductors, Cambridge, Mass. (1970).

4 V. V. Kurylev and S. N. Karyagin, Phys. Stat. Sol. (a) 21, K127 (1974).

5 S. N. Karyagin, Phys. Stst. Sol. (a) 68, K113 (1981).

6 V. A. Grazhulis, V. V. Kveder, Yu. A. Osip'yan, JETP Lett. 21, 335 (1975).

7 T. Wosinski and T. Figielski, Phys. Stat. Sol. (b) 71, K73 (1975).

8 T. Wosinski, T. Figielski, and A. Makosa, Phys. Stat. Sol. (a) 37, K57 (1976).

9 W. Szkielko, Phys. Stat. Sol. (b) 90, K81 (1978).

FOOTNOTES TO CHAPTER IV

1 E.J. Pakulis and C.D. Jeffries, Phys. Rev. Lett. 47, 1859 (1981)

2 A. Abragam and B. Bleaney, ELECTRON PARAMAGNETIC RESONANCE OF TRANSITION IONS, Clarendon Press (Oxford, 1970)

3 D.K. Wilson, Phys. Rev. 134, A265 (1964)

4 R.E. Pontinen and T.M. Sanders, Jr., Phys. Rev. 152, 850 (1966)

5 E.E. Haller and L.M. Falicov, Phys. Rev. Lett. 41, 1192 (1978)

6 V.V. Kurylev and S.N. Karyagin, Phys. Stat. Sol. (a) 21, K127 (1974)

7 S.N. Karyagin, Phys. Stat. Sol. (a) 68, K113 (1981)

8 Laura M. Roth, Phys. Rev. 118, 1534 (1960)

9 E. Weber and H. Alexander, J. Phys. (Paris), Colloq. 40, C6-101 (1979)

10 For evidence of quasi one dimensional conduction along dislocations in other materials see, for example, C. Elbaum, Phys. Rev. Lett. 32, 376 (1974) and V.A. Grazhulis, V.V. Kveder, V. Yu. Mukhina, and Yu. A. Osip'yan, JETP Lett. 24, 142 (1976).

11 R.E. Peierls, Quantum Theory of Solids, Lecture Notes (1953)

12 I.S. Jacobs et al, Phys. Rev. B 14,3036 (1976)

13 P. Pincus, Solid State Commun. 9, 1971 (1971).

14 V.A. Grazhulis, V.V. Kveder, and Yu.A. Osip'yan, Phys. Stat. Sol. (b) 103, 519 (1981)

FOOTNOTES TO CHAPTER V

1 H. Reiss, C.S. Fuller, and F.J. Morin, Bell Syst. Tech. J. 35, 535 (1956).

2 R.L. Aggarwal, P. Fisher, V. Mourzine, and A.K. Ramdas, Phys. Rev. 138, A882 (1965).

3 R.J. Fox, IEEE Trans. Nucl. Sci. 13, 367 (1966).

4 E.M. Bykova, L.A. Goncharov, T.M. Lifshits, V.I. Sidorov, and R.N. Hall, Fiz. Tekh. Poluprov. 9, 1966 (1975) (Sov. Phys. Semicond. 9, 1228 (1976)).

5 E.E. Haller and L.M. Falicov, Phys. Rev. Lett. 41, 1192 (1978).

FOOTNOTES TO CHAPTER VI

1 U. Schmidt, E. Weber, H. Alexander, and W. Sander, Solid State Commun. 14, 735 (1974).

TABLE II.1 - LIST OF FILTERS

Germanium filter - 2 mm thick

Neutral density filters - 3, 10, 20, 30 dB

Long wavelength pass filters -

	5% Wavelength	50% Wavelength	Transmission	Material	Size	Thickness
A	3.4600	3.5400	90%	Ge	1"D	.040"
B	2.9000	2.9495	63%	Ge	1"D	.037"
C	2.4340	2.5087	80%	Saphire	1"D	.060"
D	2.0500	2.1100	80%	Glass	1"D	.040"

Wavelengths in microns.

Transmission at maximum.

Long pass filters purchased from Valtec Corporation.

TABLE II.2 - SAMPLE CHARACTERISTICS

Boule Number	Growth Axis	Atmosphere	Crucible	Dimensions Shape	Orientation	N_D-N_A (cm^{-3})	Etchpits (cm^{-2})	Donor
S-17	<100>	H_2	Quartz	12.5mmD C 8x10x10mm R 6x8x10mm R	<100> <100> <110>	8×10^{13}	2×10^4	As
S-29	<100>	H_2	Quartz	12.5mmD C	<110>	7×10^{12}	0	As
S-61	<100>	H_2	Quartz	12.5mmD C	<110>	2×10^{12}	2×10^3	As
S 62	<100>	H_2	Quartz	12.5mmD C	<110>	1×10^{12}	2×10^3	As
464	<100>	H_2	Quartz	12.5mmD C	<100>	3×10^{12}	6×10^3	P,As
574	<100>	H_2,D_2 1:1	Quartz	12.5mmD C	<110>	5×10^9	5×10^4	?
518	<100>	D_2	Quartz	12.5mmD C	<110>	1×10^{12}	1×10^4	P
139	<100>	Vacuum	Quartz	12.5mmD C	<110>	2×10^{12}	1×10^4	P
400	<111>	Ar	Graphite	4x10x11mm R	<110>	4×10^{12}	5×10^3	P
370	<100>	H_2	Quartz	12.5mmD C	<110>	1×10^{13}	1×10^4	Li

C: Right circular cylinder R: Rectangular parallelepiped D: Diameter

TABLE IV.1 - SPECTROSCOPIC SPLITTING FACTOR IN Ge

CENTER	$g_\perp$	$g_\parallel$	g_{iso}*	g<100>	Reference
4-line spectrum	1.94	0.34		1.59	IV.1
24-line spectrum	1.89	0.73		1.60	IV.1
Substitutional P	1.93^s	0.83^s	1.563	1.647	IV.3
Substitutional As	1.92^s	0.87^s	1.570	1.647	IV.3
Substitutional Sb				1.561	IV.4
Substitutional Bi			1.567		IV.3
Surface Sb	1.917	0.83		1.636	IV.4
LiO Complex	1.91	0.85		1.63	IV.5
Intrinsic Surface State 1			2.008		IV.6,7
Intrinsic Surface State 2			2.003		IV.6,7
Conduction Electron	2.07^c	0.98^c	1.71^c	1.78^c	IV.8

s: Determined from experiments on stressed crystals.
c: Calculated values.
*: Isotropic value $g_{iso}=1/3g_\parallel+2/3g_\perp$

FIGURE CAPTIONS CHAPTER I

Figure I.1 Dislocations of the screw and edge types.

Figure I.2 Germanium crystal structure including one 60° -dislocation line,d, with its row of dislocation dangling bonds, and Burgers vector, $\vec{b}$. See reference I-7.

FIGURE CAPTIONS CHAPTER II

Figure II.1 Block diagram of the apparatus.

Figure II.2 Dimensions of the interior of the helium dewar. The inner can is surrounded by a vacuum and a liquid nitrogen shield (not shown).

Figure II.3 Dewar insert showing waveguide, radiation shields, stainless steel tuning and coupling rods, microwave cavity, and aluminum shutter.

Figure II.4 Blowup of the tunable cavity showing position of sample.

Figure II.5 The two experimental geometries used. The orientation of the four <111> axes relative to the plane of rotation of the magnetic field is indicated for (a) $\vec{H}$ in (110) plane, and (b) $\vec{H}$ in (100) plane.

FIGURE CAPTIONS TO CHAPTER IV

Figure IV.1 Derivative curves of EPR in As doped Ge (Boule S-17, $N_D - N_A = 8 \times 10^{13}$ cm^{-3}). Magnetic field is oriented along a <100> direction. T = 2 K, f = 25.16 GHz. Note the sign reversal of the new lines as compared to the As hyperfine structure. Dislocation density ∿2 X 10^4 cm^{-2} .

Figure IV.2 Angular dependence of the g-tensor for the narrow new lines in a sample of P doped Ge (Boule 518, $N_D - N_A = 10^{12}$ cm^{-3}) as the magnetic field is rotated in a plane tilted ∿3° from a (110) plane. Insert shows the continuation of the lines for low values of g near <110>. No data were taken for g<1, corresponding to H>19 kG, the limit of the magnet used. T = 2K, f = 26.06 GHz, dislocation density ∿10^4 cm^{-2} . The dashed line shows a portion of one of the four broad lines.

Figure IV.3 Angular dependence of the g-tensor for the narrow lines in a sample of As doped Ge (Boule S-17, $N_D - N_A = 8 \times 10^{13}$ cm^{-3}) as the magnetic field is rotated in a plane tilted ∿3° from a (100) plane. Insert shows the continuation of the lines for low values of g near <110>. T = 2K, f = 24.37 GHz, dislocation density ≈ 2 X 10^4 cm^{-2} . The dashed lines show parts of two of the four broad lines.

Figure IV.4 Angular dependence of the g-tensor for the four broad lines in a sample of As doped Ge (Boule S-17, $N_D - N_A = 8 \times 10^{15}$ cm^{-3}) as the magnetic field is rotated in the (100) plane. T = 2K, f = 24.36 GHz, dislocation density $\approx 2 \times 10^4$ cm^{-2}.

Figure IV.5 Plot of g^2 vs $\cos^2\theta$ for the four broad lines, where θ is the angle between $\vec{H}$ and a <111> axis. The straight line means g is axially symmetric about the <111>'s. $g_\parallel = 0.34$ and $g_\perp = 1.94$.

Figure IV.6 Computer simulation of the 24 line spectrum for $\vec{H}$ in the (110) plane.

Figure IV.7 Computer simulation of the 24 line spectrum for $\vec{H}$ in the (100) plane.

Figure IV.8 Dependence of line shape on excitation intensity, (a) ten times the intensity of (b).

Figure IV.9 Comparison of the amplitudes of the arsenic hyperfine structure (—o—) and the dislocation lines (—x—) as long pass filters of successively higher energies are used. Filters are indicated along the energy axis at their 50% wavelength energy.

Figure IV.10 Effect of microwave power on the broad lines. (a) 5×10^{-9} watts. (b) 5×10^{-7} watts.

Figure IV.11 Effect of microwave power on the narrow lines. (a) 5×10^{-9} watts. (b) 5×10^{-8} watts.

Figure IV.12 log Amplitude vs time after closing optical shield. (x) boule 139 (.) boule S-17 (o) arsenic hyperfine structure for comparison.

Figure IV.13 Spin dependent scattering of photo excited electrons (bold arrows) by dangling bonds along a dislocation line.

Figure IV.14 Projection of the Ge crystal structure onto the (111) plane. The heavy labelled lines are the <110> axes in that plane. The six arrows, not to scale, are projections of six of the symmetry directions of the g-tensor for the narrow new lines.

Figure IV.15 Several possibilities for the projection of the dislocation dangling bonds onto the (111) plane. The dashed lines are dislocations.

Figure IV.16 Energy bands for a linear chain of atoms, one electron per site, for (a) uniform spacing "a" (b) dimerized chain, lattice spacing "2a".

FIGURE CAPTIONS – CHAPTER V

Figure V.1 Angular dependence of the EPR lines observed for the lithium diffused Ge sample (Boule 370) containing dislocations as the magnetic field is rotated in the approximate (110) plane. Insert shows the continuation of the lines for low values of g near <110>. $N_D - N_A \approx 10^{13}\ cm^{-3}$. *Dislocation density* $\sim 10^3\ cm^{-2}$. T=2 K. f=23.49 GHz. Points are measured values. Lines are computer simulation based on perfect crystal alignment and g values quoted in the text. Solid lines: lithium at dislocations. Dashed lines: LiO complex. Deviations from calculations can be accounted for by assuming a misorientation of ≈1°. Note that lines degenerate for perfect alignment can become resolved for other orientations.

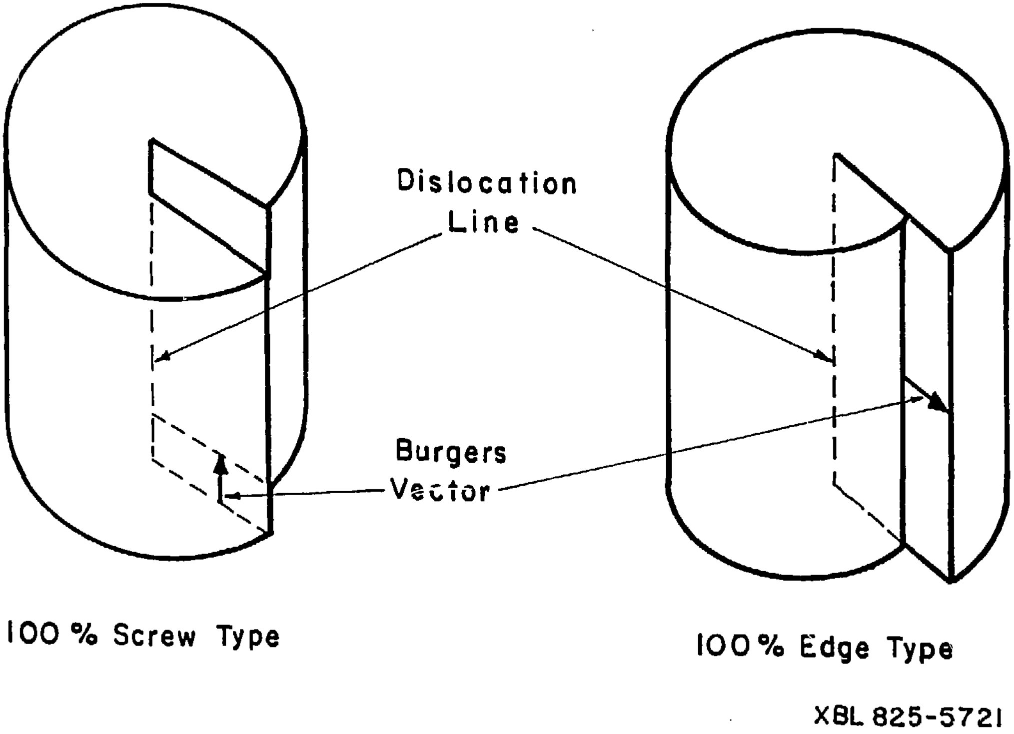
Dislocation Line
Burgers Vector
100 % Screw Type
100 % Edge Type
XBL 825-5721

Fig. I.1

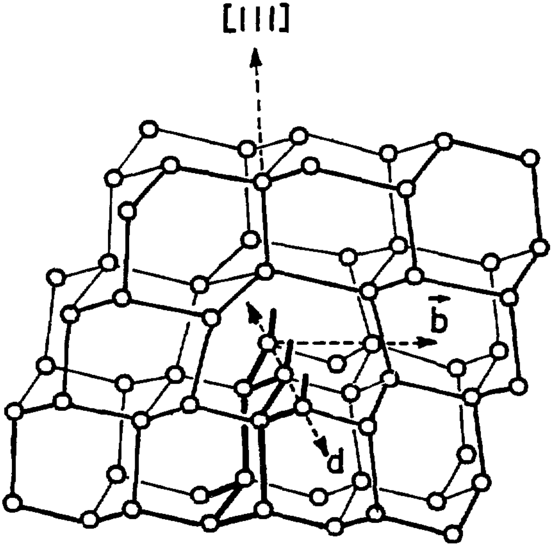

Fig. I.2

APPARATUS

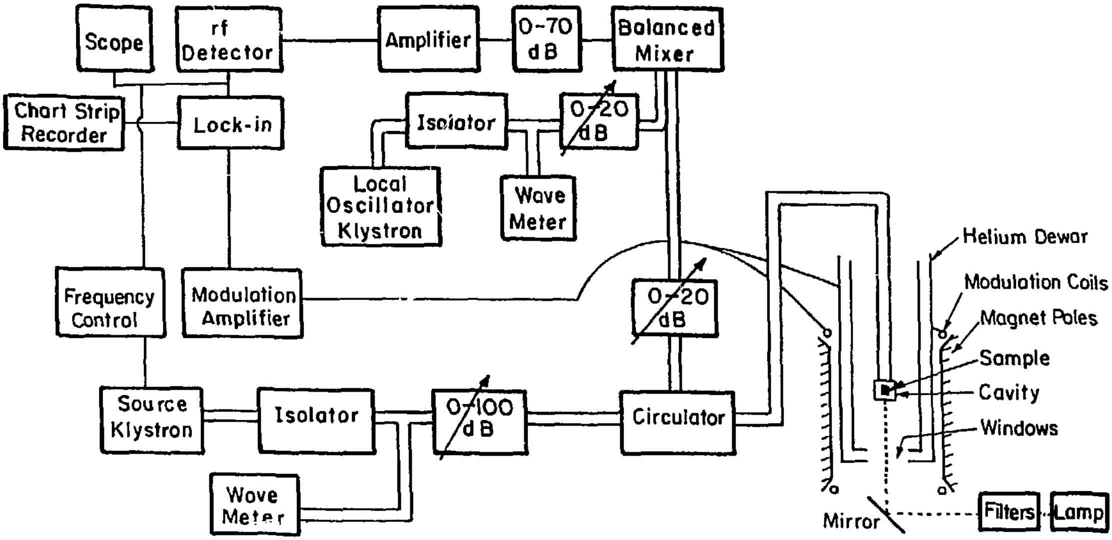

XBL825-5722

Fig. II.1

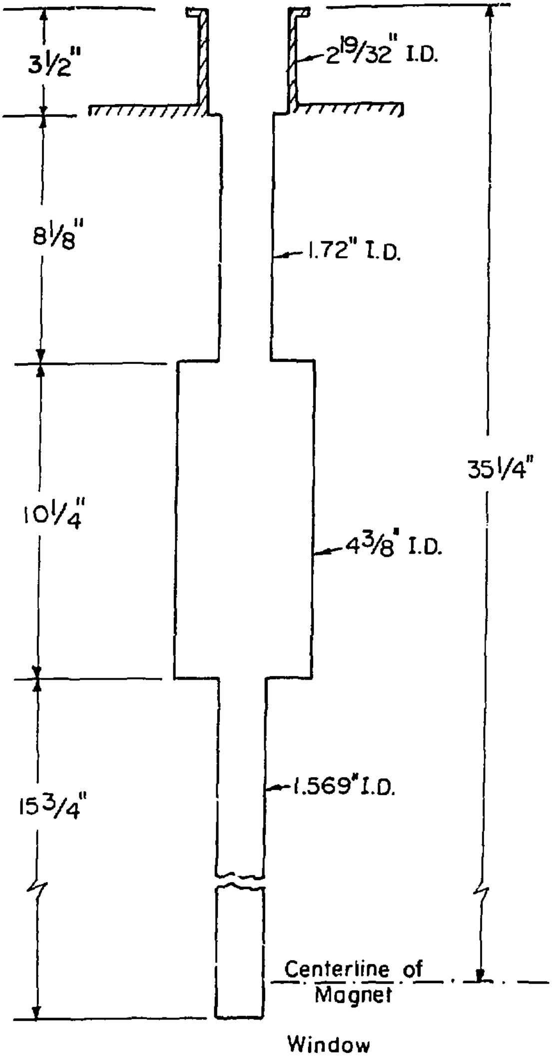

XBL 826-5859 Fig. II.2

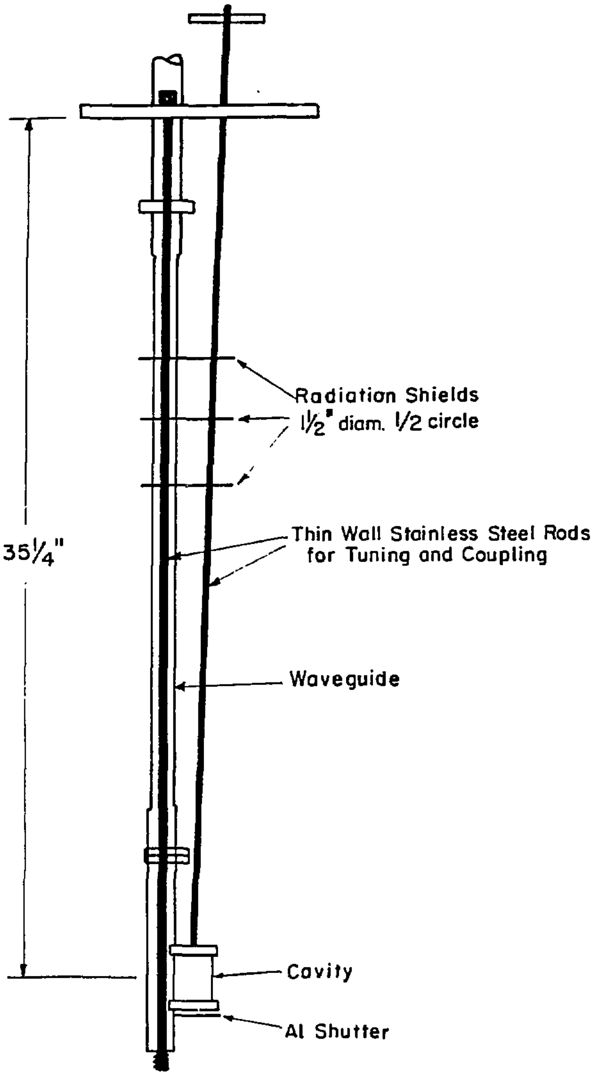

Fig. II.3 XBL 825-5723

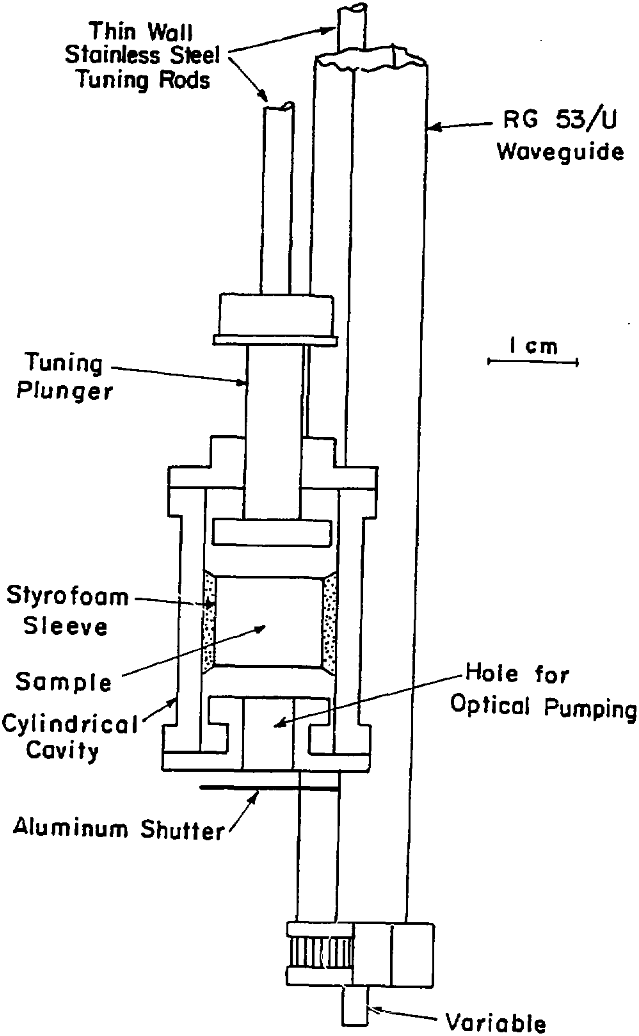

Fig. II.4

XBL 825-5724

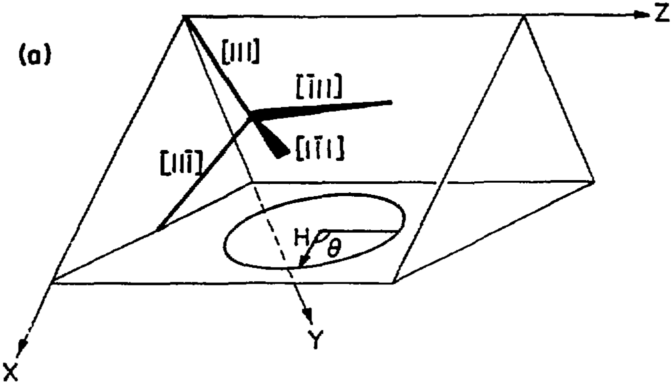

Magnetic Field in (110) Plane

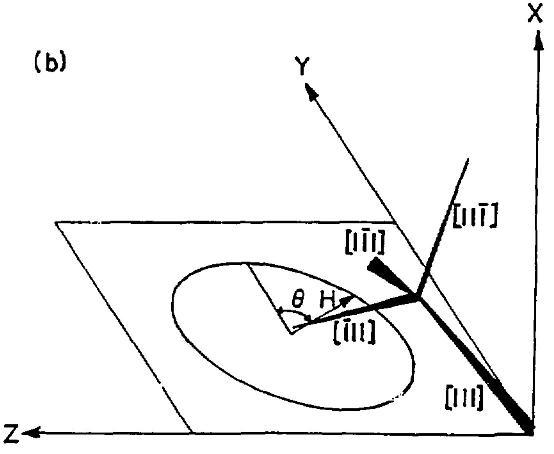

Magnetic Field in (100) Plane

Fig. II.5

XBL 825-5725

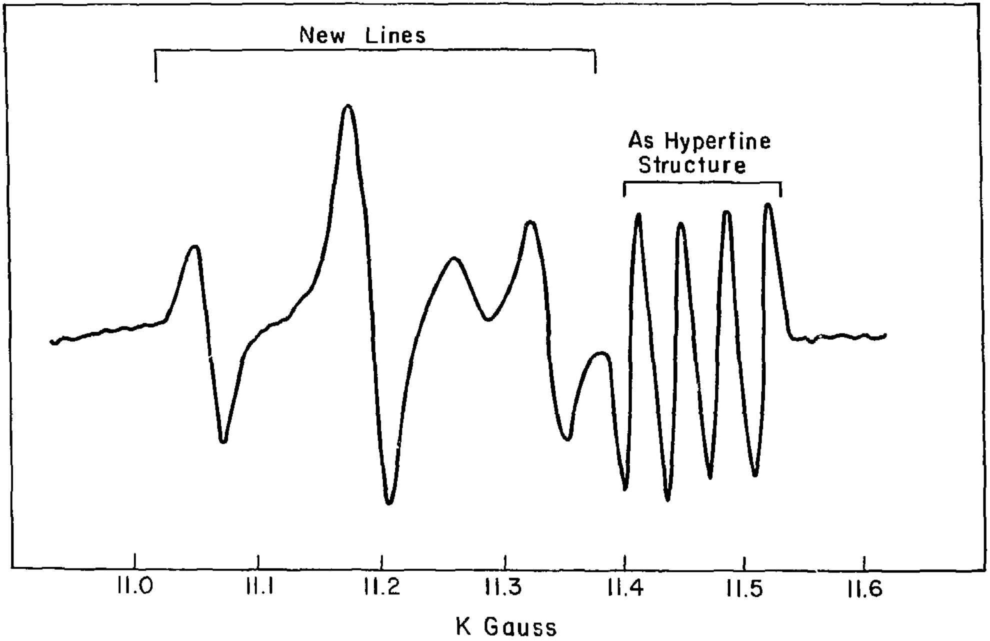

XBL 811-107

Fig. IV.1

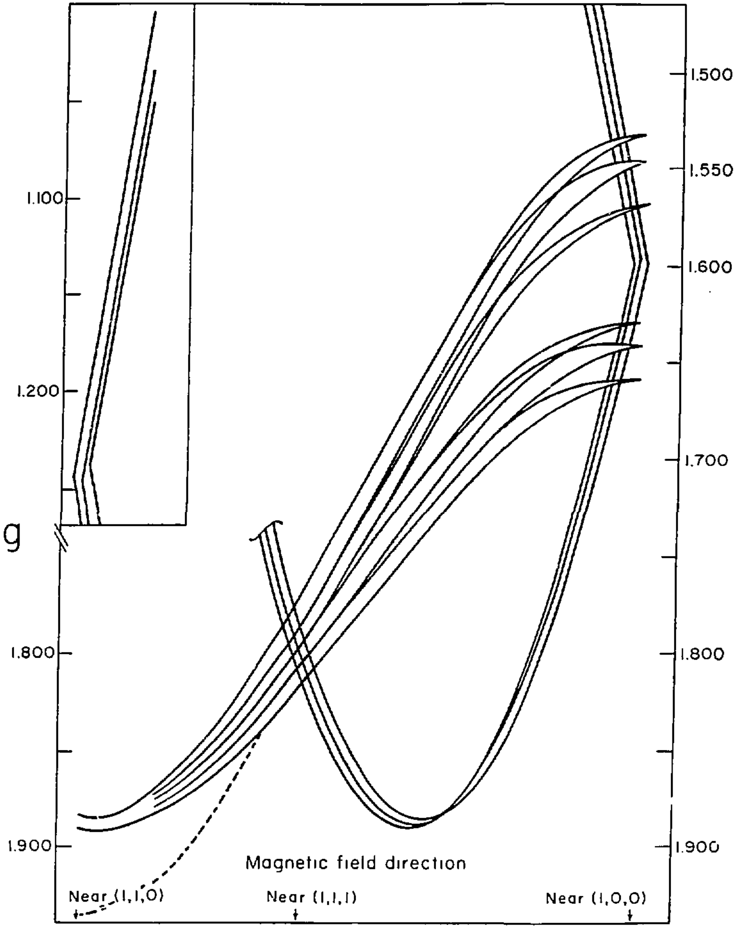

XBL 811-108

Fig. IV.2

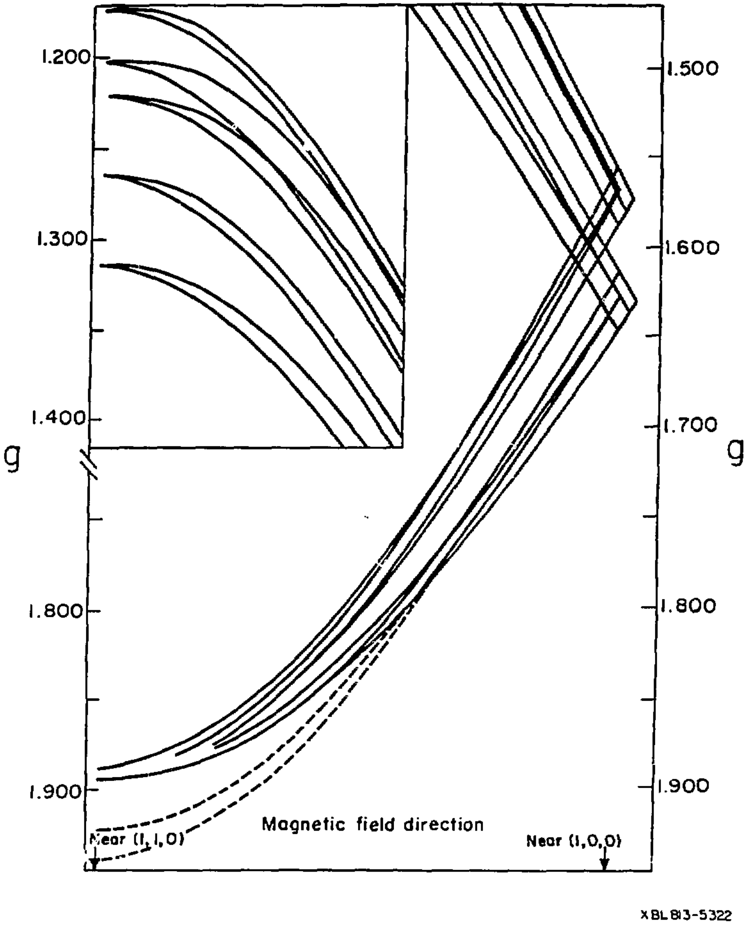
1.200
1.300
1.400
g
1.800
1.900
1.500
1.600
1.700
g
1.800
1.900
Magnetic field direction
Near (1,1,0)
Near (1,0,0)
XBL 813-5322

Fig. IV.3

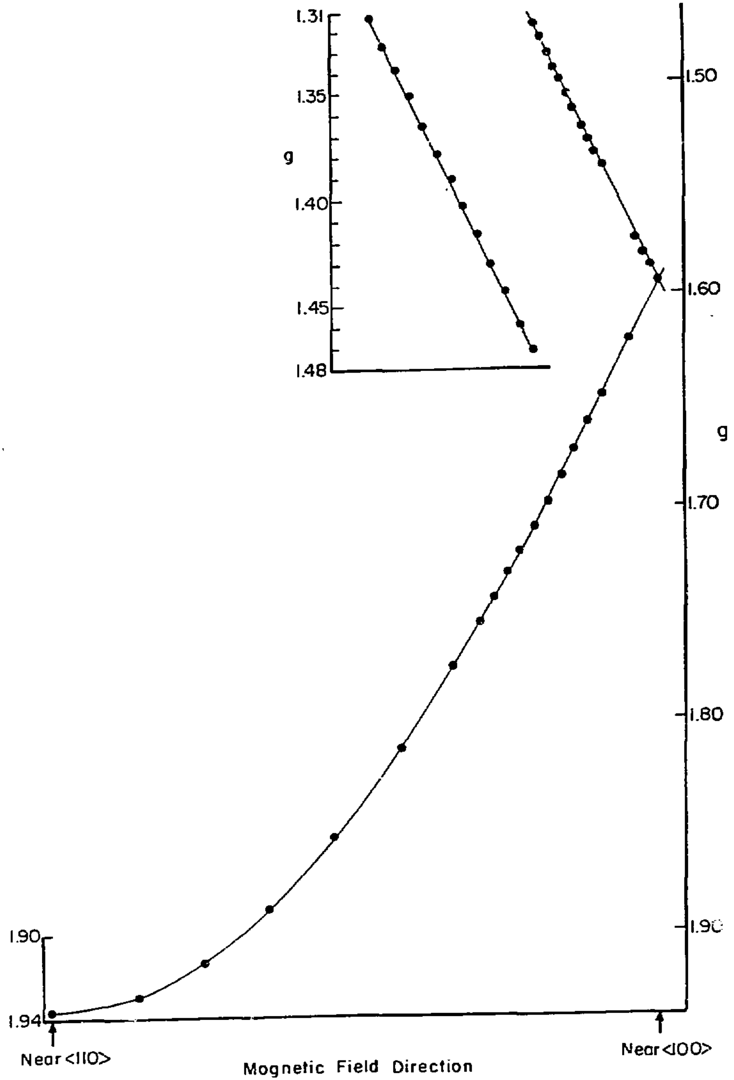
1.31
1.35
1.40
1.45
1.48
g
1.50
1.60
g
1.70
1.80
1.90
1.90
1.94
Near <110>
Near <100>
Magnetic Field Direction
XBL 826-5889

Fig. IV.4

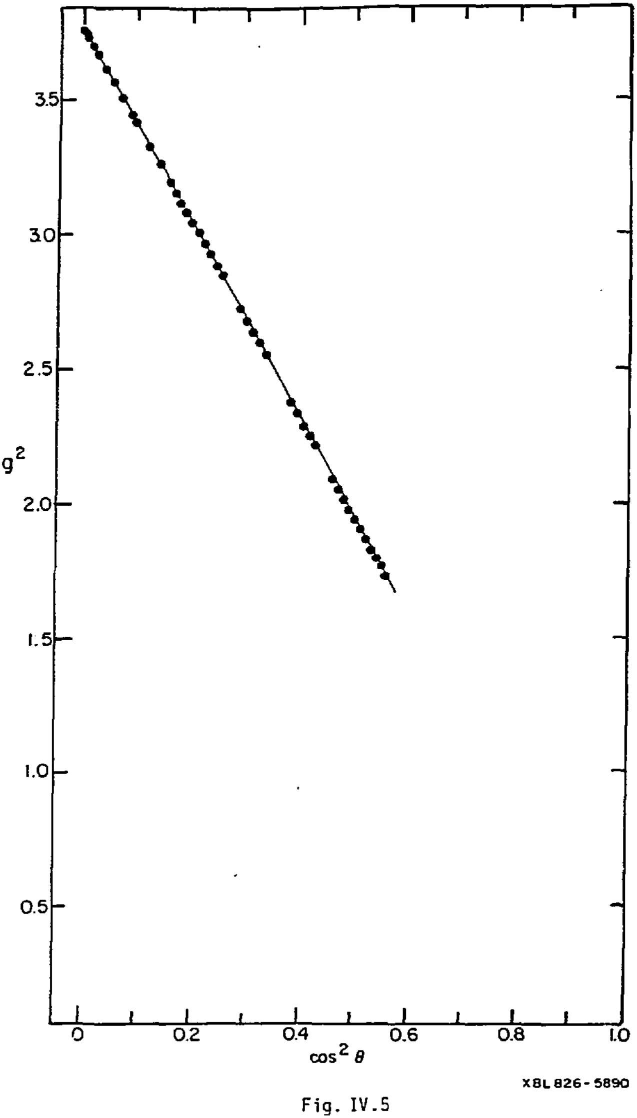

Fig. IV.5

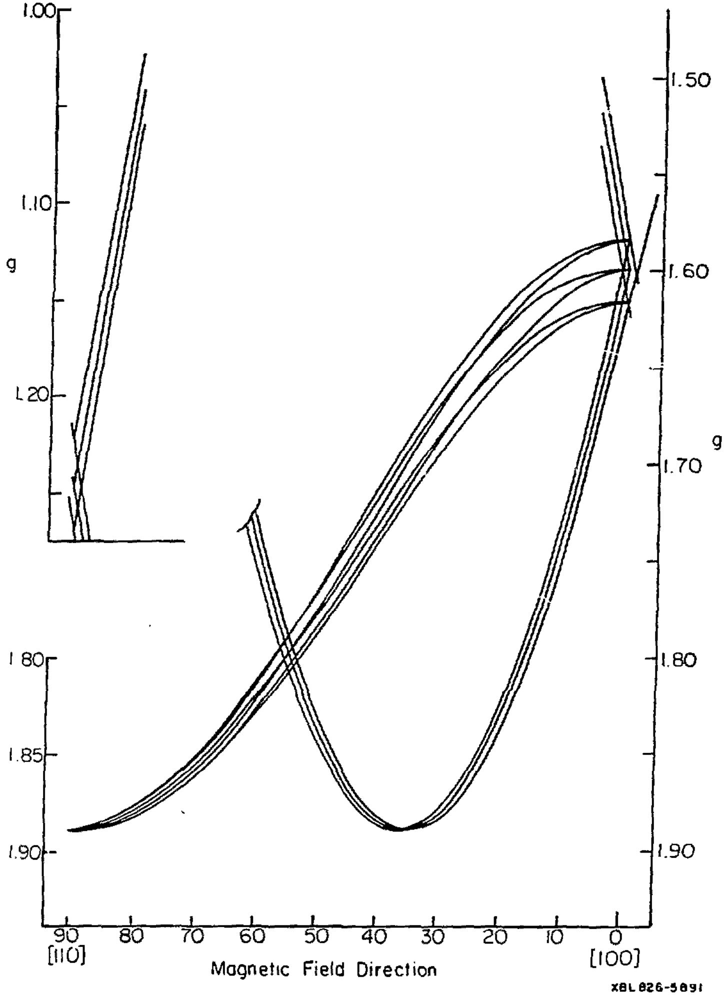
1.00
1.10
g
1.20
1.80
1.85
1.90
1.50
1.60
g
1.70
1.80
1.90
90
[110]
80
70
60
50
40
30
20
10
0
[100]
Magnetic Field Direction
XBL 826-5891

Fig. IV.6

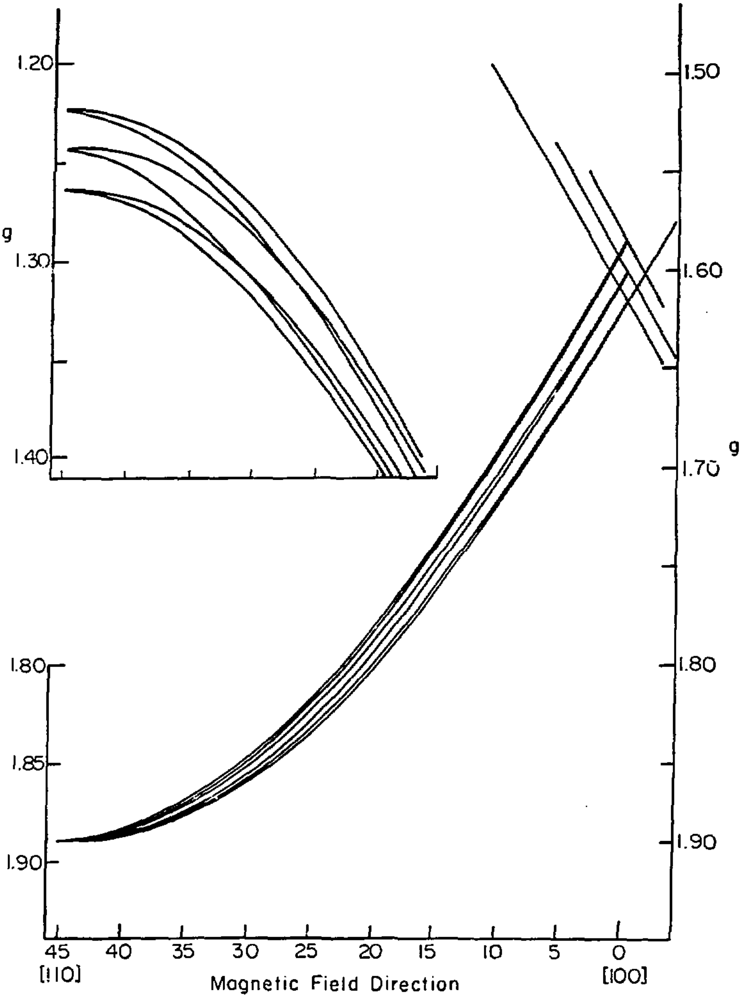

XBL826-5892

Fig. IV.7

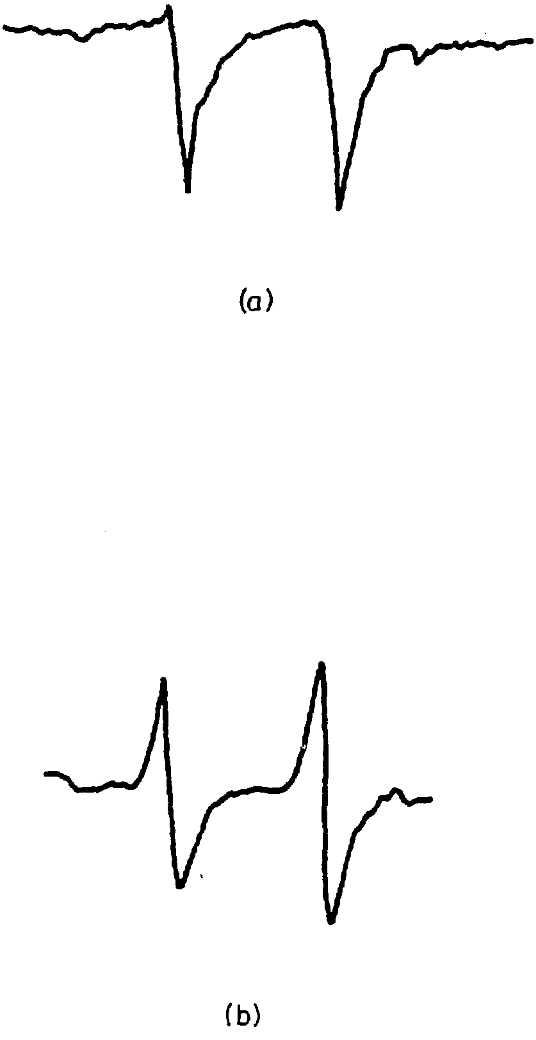

Fig. IV.8 XBL 826-5882

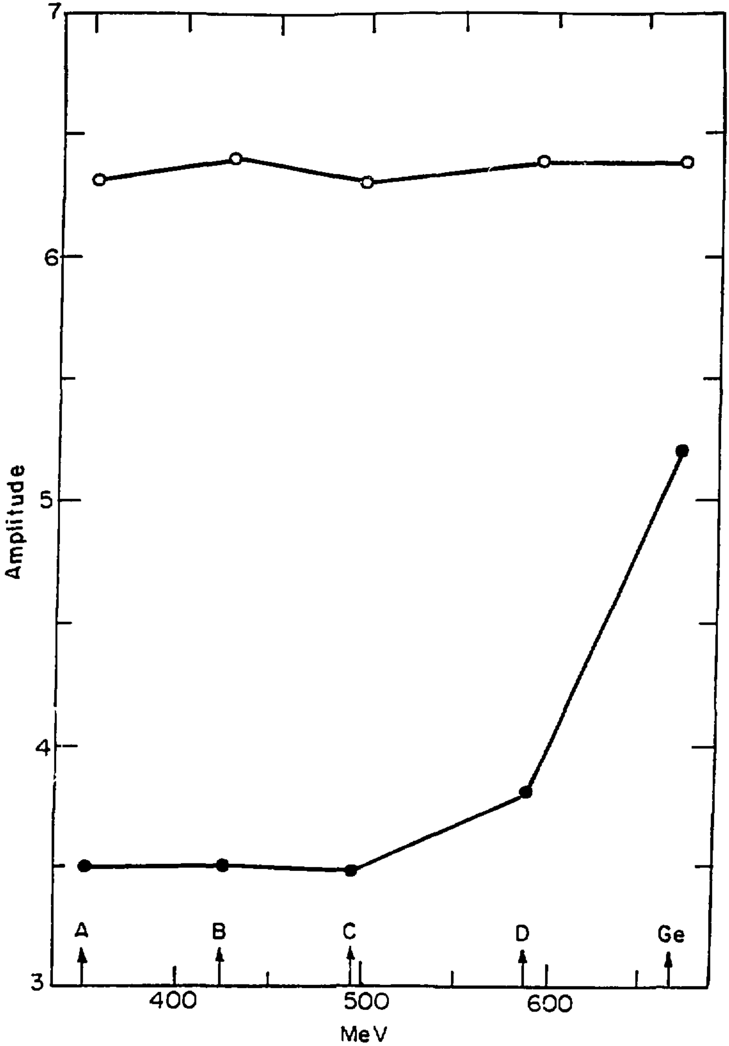

XBL 826-5883

Fig. IV.9

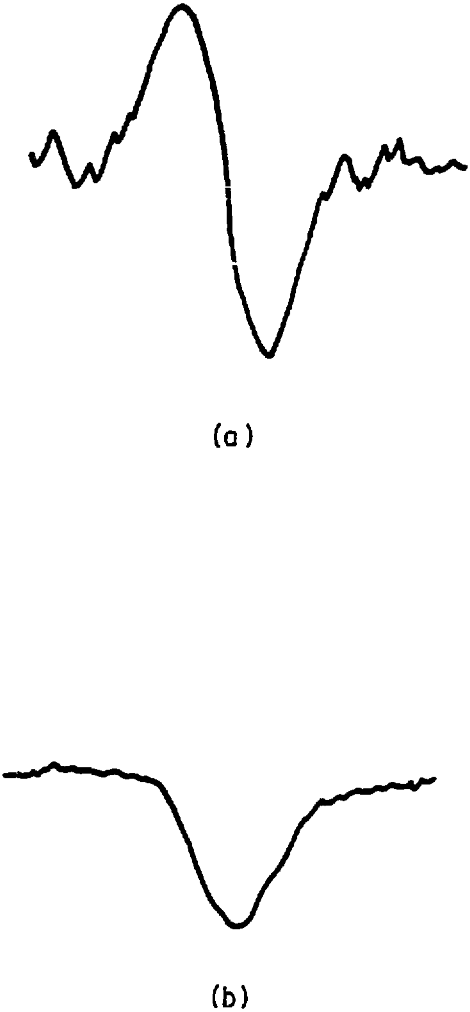

XBL826-5884 Fig. IV.10

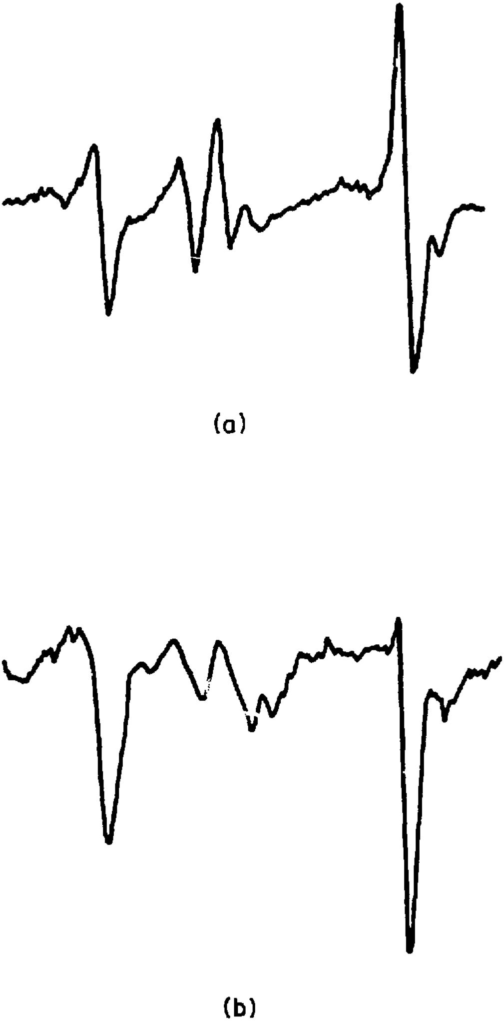

Fig.IV.11 XBL826-5885

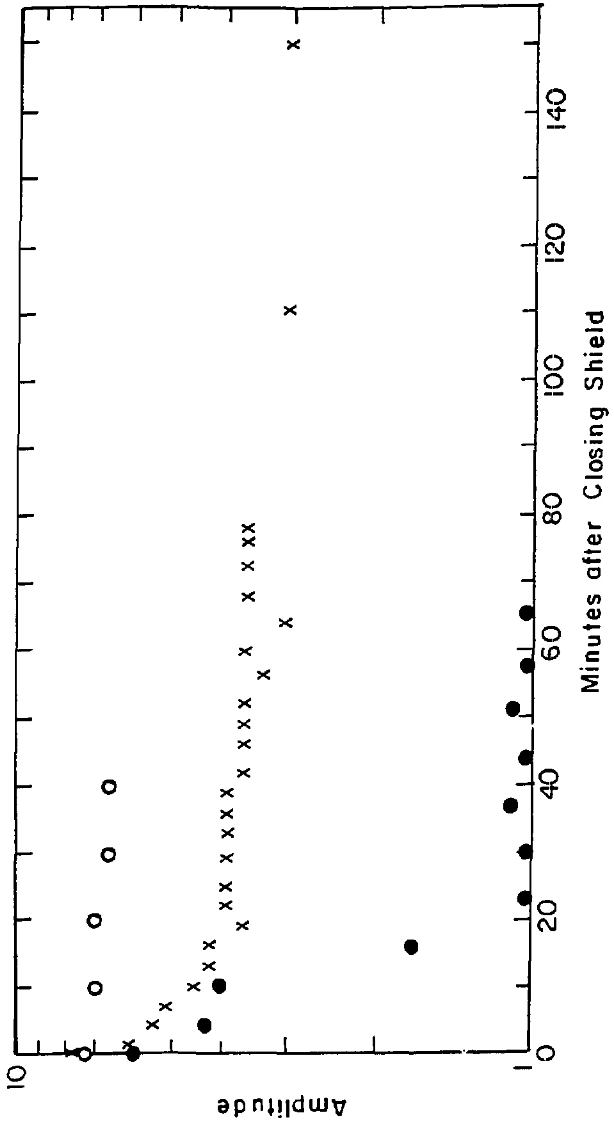

XBL 826-5886

Fig. IV.12

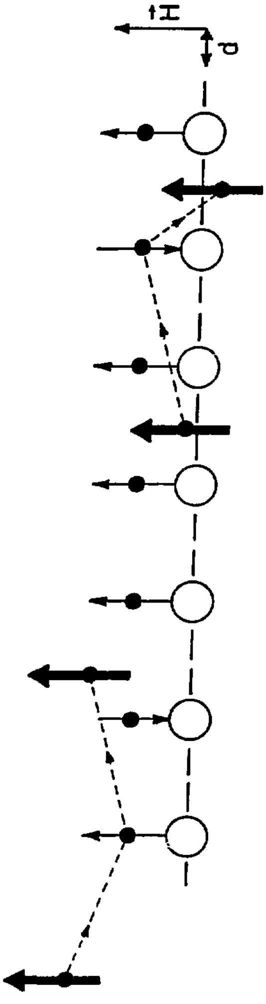

XBL 8111-12859

Fig.IV.13

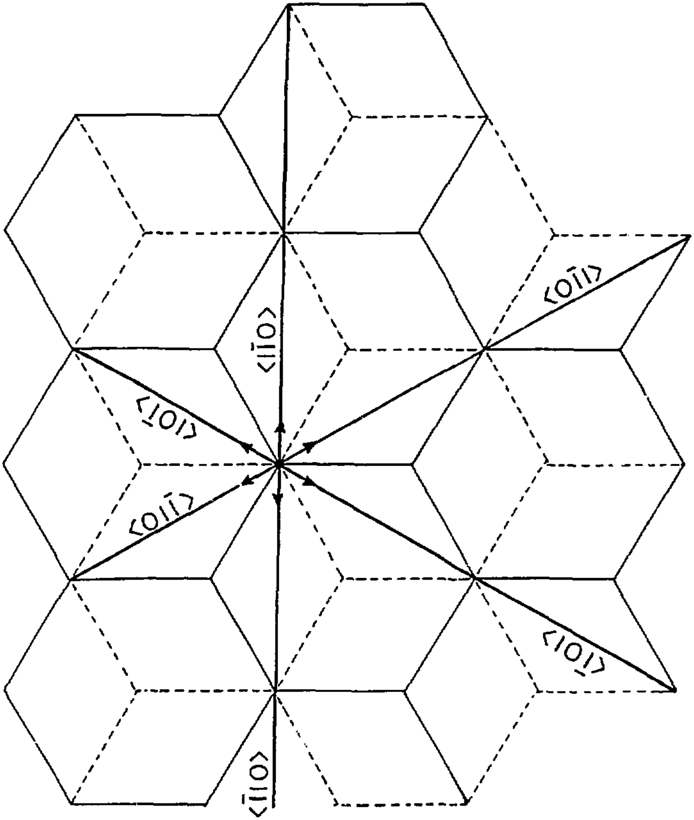

XBL 819-6500

Fig. IV.14

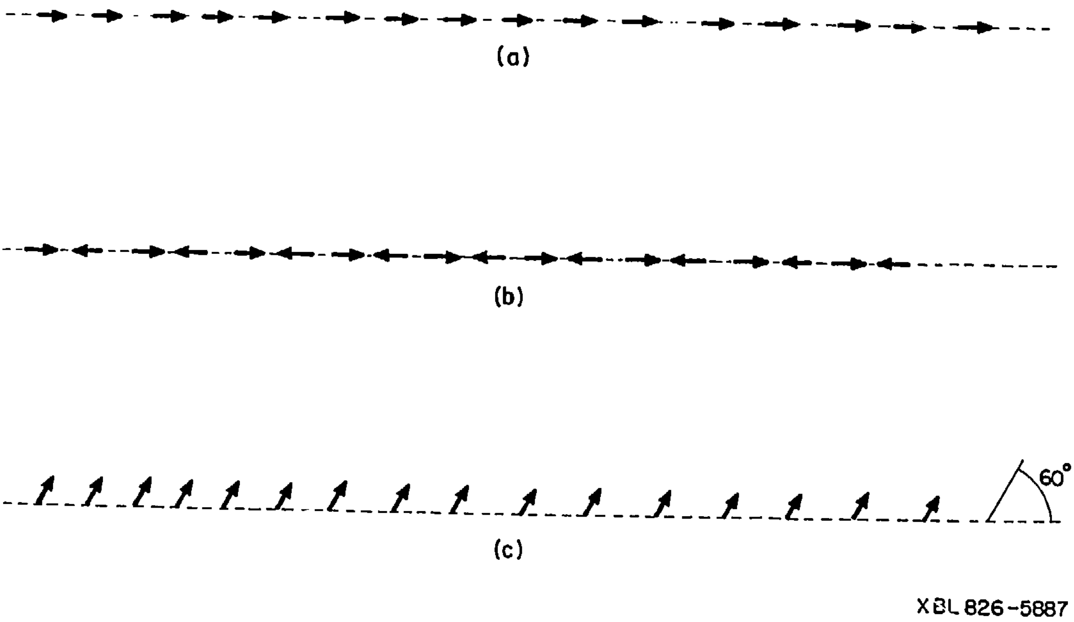

Fig.IV.15

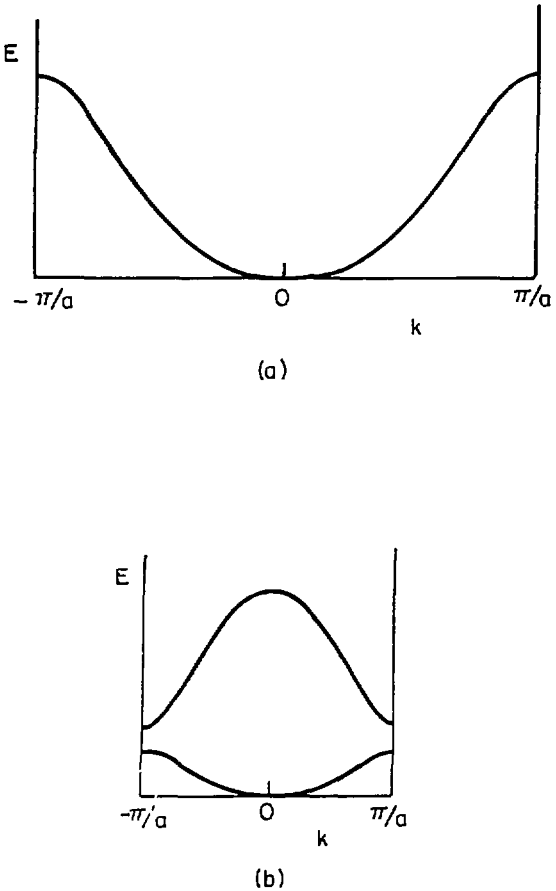

XBL 826-5888

Fig. IV.16

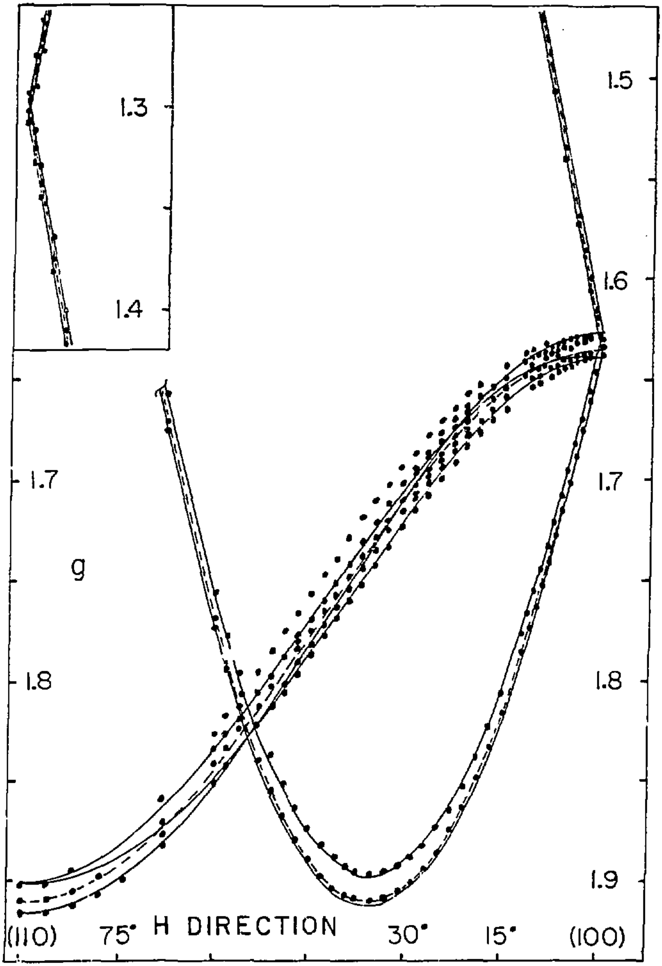

XBL 826-10393

Fig.V.1

END

DATE FILMED
9-29-82